Effective stress analysis of residual wave-induced liquefaction around caisson-foundations

Bearing capacity degradation and an AI-based framework for predicting settlement

Moghaddam, Amir; Barari, Amin; Farahani, Sina; Tabarsa, Alireza; Jeng, Dong-Sheng

Published in:
Computers and Geotechnics

DOI (link to publication from Publisher):
10.1016/j.compgeo.2023.105364

Publication date:
2023

Document Version
Publisher's PDF, also known as Version of record

Computers and Geotechnics 159 (2023) 105364

Contents lists available at ScienceDirect

Computers and Geotechnics

journal homepage: www.elsevier.com/locate/compgeo

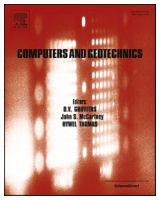

Effective stress analysis of residual wave-induced liquefaction around caisson-foundations: Bearing capacity degradation and an AI-based framework for predicting settlement

Amir Moghaddam [a,b], Amin Barari [a,c,*], Sina Farahani [a,d], Alireza Tabarsa [b], Dong-Sheng Jeng [e]

[a] Department of the Built Environment, Aalborg University, Thomas Manns Vej 23, 9220 Aalborg Ø, Denmark
[b] Department of Civil Engineering, Faculty of Engineering, Golestan University, Gorgan, Iran
[c] School of Engineering, RMIT University, Melbourne, VIC 3000, Australia
[d] Department of Civil Engineering, Razi University, Kermanshah, Iran
[e] School of Engineering and Built Environment, Griffith University Gold Coast Campus, Queensland 4222, Australia

ARTICLE INFO

Keywords:
Wave-induced liquefaction
Suction caisson foundation
Offshore wind turbine
Bearing capacity
Settlement
Artificial intelligence

ABSTRACT

Excessive wave-induced pore pressure buildup around offshore foundations results in liquefaction, settlement and bearing capacity degradation, which may threaten the safety of Offshore Wind Turbines (OWTs). Despite the extensive research efforts on wave-induced seabed residual response in the recent years, there is still a lack of knowledge on mechanisms of wave-induced liquefaction and settlement around caisson foundations. Employing a code-based framework implemented in OpenSees, the cyclic response of wave-seabed-foundation (WSF) system is evaluated. Biot's consolidation theory, linear wave theory and CycLiqCPSP constitutive soil model are integrated to evaluate the response of soil-foundation system accounting for the hydrodynamic pressure of wave imposed on the seabed surface considering the fully-coupled wave-seabed-foundation interaction (WSFI). Soil model parameters are calibrated against cyclic simple shear (CSS) tests and the numerical model is validated by a well-documented centrifuge experimental model. Various seabed characteristics, and a range of the geometrical properties of foundation with different OWT weights are put into practice for evaluating the geotechnical aspects of wave-induced liquefaction. Stress paths are provided to demonstrate quite different level of reduction in effective stresses and likelihood of liquefaction occurrence upon cyclic shear stresses application for different locations in the vicinity of the foundation area. The present study will also improve understanding of the interplay among the state variables on the wave-induced foundation settlement and bearing capacity degradation allow to feed the output data into development of simplified procedure for assessing the bearing capacity. Finally, results from over 250 analyses with different model configurations are used to provide an estimate of wave-induced caisson settlement with reasonable accuracy on the basis of artificial intelligence (AI) method known as Group Method of Data Handling (GMDH).

1. Introduction

Recent studies demonstrated that caisson foundation is an economically suitable solution as foundation for offshore wind turbines (Bienen et al., 2012; Achmus et al., 2013; Ibsen et al., 2014a, 2014b; 2015; Barari and Ibsen, 2017; Skau et al., 2018; Suryasentana et al., 2020; Stapelfeldt et al., 2020, 2021). Caisson is a large, thin-walled hollow cylinder, which is closed at the top and open at the bottom. In comparison with traditional offshore pile, the caisson foundation has some substantial advantages including its higher horizontal and lateral loading capacity, environment-friendly setup (slightly less sound pollution and reduced vibration), adaptability to varying offshore soil conditions, and accurate positioning.

In the past decade, due to the wide applications of suction caisson foundations and the vital role it plays for the construction of offshore structures, numerous experimental work has been conducted to assess suction caissons' performance under cyclic loading (Barari and Ibsen, 2017; Zhu et al., 2019). Advanced constitutive models have also been used for cyclic and seismic response of offshore foundations (Gelagoti et al., 2014; Kourkoulis and Georgiou, 2015; Barari et al., 2021a;

* Corresponding author.
E-mail addresses: amir.moghaddam93@gmail.com (A. Moghaddam), amin.barari@rmit.edu.au (A. Barari), farahani.sina@razi.ac.ir (S. Farahani).

https://doi.org/10.1016/j.compgeo.2023.105364
Received 15 November 2022; Received in revised form 13 February 2023; Accepted 22 February 2023
Available online 1 April 2023

Tasiopoulou et al., 2021; Liu et al., 2021); While some research has been carried out on the earthquake-induced soil liquefaction and its impact on the caisson foundations performance supporting OWTs (Wang et al., 2017; Esfeh and Kaynia, 2020; Haddad et al., 2022; Palacios et al., 2022), very little has been reported on their interaction with wave-induced liquefied seabed (Zhang et al., 2016).

It is critically important for geotechnical engineers to evaluate the stability of offshore foundations in harsh conditions of marine environment. When waves propagate on the surface of sea, they impose hydrodynamic pressure on seabed. These cyclic fluctuations generate excess pore pressure that have been identified as a major factor in analyzing the seabed instability around offshore foundations. If the pore pressure reaches the limit value, the effective stress in seabed vanishes which causes the seabed soil to liquefy. To avoid this instability around offshore foundations, it is necessary to study the cyclic behavior of seabed under harsh conditions and in the presence of structure.

Based on in-situ investigations and experimental observations, two mechanisms for wave-induced liquefaction have been identified (Zen and Yamazaki, 1990), which are momentary liquefaction and residual liquefaction. The former is caused by the transient excess pore water pressure when the wave-trough moves on the surface of sea water. Wave-induced pore pressure generates large upward pressure gradients on seabed surface and can transitorily liquefy the soil if the lift induced by upward seepage force surpasses the specific weight of the seabed soil (Yamamoto et al., 1978), while the other is due to the buildup of excess pore water pressure in partially drained or undrained soils caused by the cyclic shearing and the subsequent volumetric contraction in soil mass (Seed and Rahman, 1978). Residual wave-induced liquefaction is therefore related to the Elasto-plastic behavior of soil. Moreover, assessing the seabed response in the presence of marine structures is more sophisticated because of the influence of initial stress distribution induced by soil-foundation interaction (SFI) (i.e., initial confining pressure and static shear stress). In the past few years, most of the WSFI studies have focused on the seabed response under the action of waves around gravity-based foundations (Li et al., 2018) and pile foundations (Sumer, 2014; Zhang et al., 2015; Zhao et al., 2017; Zhu et al., 2018; Sui et al., 2019).

In the recent years, several meshfree methods have been implemented in numerical models experiencing large deformations, especially landslide run-out simulations. Bandara et al. (2016) examined the pre- and post-failure response of landslides in unsaturated slopes resulted from rainfall infiltration based on material point method. Wei et al. (2020) employed the naturally stabilized nodal integration (NSNI) to reach an efficient and steady reproducing kernel mixed formulation to demonstrate failure model of a partially saturated levee. Expanding on this idea, the installation and operation of suction caissons in offshore environment may serve as a base for using material point method (MPM) and reproducing kernel particle method (RKPM). However, the development of a corresponding methodology falls out of the scope of this study.

This paper evaluates the consequence of wave-induced residual liquefaction around suction caisson foundations considering WSFI (Fig. 1), using a novel, code-based framework implemented in OpenSees, the finite element software, originally programmed for dynamic SSI (McKenna et al., 2000). The CycLiqCPSP model developed by Wang et al. (2014), based on the work of Zhang and Wang (2012) was employed to capture the nonlinear elasto-plastic behavior of layered sandy seabed soil under the action of waves. Biot's consolidation theory, linear wave theory and the advanced soil model were eventually combined to capture the nonlinear response of soil. This finite element numerical methodology was validated using well-documented centrifuge experimental results available in the technical literature. The parameters evaluated in this research are: 1) seabed properties including specific density and thickness of the liquefiable layer; 2) geometrical properties of caisson foundation including skirt length, diameter and whether or not the skirt tip is penetrated into the liquefiable layer; 3) weight of OWT causing different contact pressures. Finally, influence of the above parameters on liquefaction triggering and stress path,

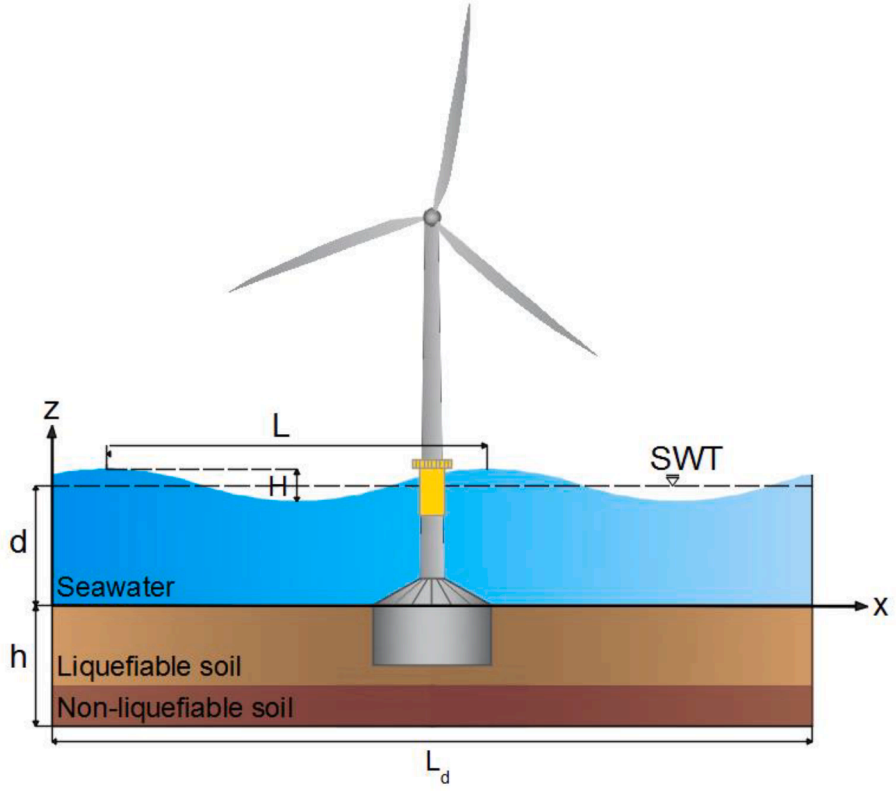

Fig. 1. A sketch for the wave-seabed-foundation interaction in the presence of offshore wind turbine.

settlement pattern and bearing capacity of foundation were examined and a functional form was introduced for assessment of bearing capacity degradation based on the excess pore water pressure ratio (r_u) generated under various wave characteristics.

Also, in spite of the extensive research conducted to estimate the earthquake-induced settlement of shallow foundations (Karimi et al. 2018), the litearture is scarse in terms of wave-induced caisson settlement in offshore environment. In the final section of this paper, over 250 finite element dynamic analyses are performed with the aid of HPC (high performance computing) facilities to demonstrate the influence of various model configurations on caisson settlement. In order to develop an analytical framework estimating the settlement of offshore suction caisson foundation under the action of sea waves, an artificial intelligence based (AI-Based) method is put into practice known as Group Method of Data Handling (GMDH) using the repetition of a series of multilayered perceptron type network structures.

2. Theoretical formulation

2.1. Governing equations

As shown in Fig. 2, the wave-induced excess pore water pressure consists of two components (Zen and Yamazaki, 1990), expressed as follows:

$$p = p_{mom} + p_{res} \tag{1}$$

In which p is wave-induced excess pore pressure, p_{mom} is momentary component and p_{res} is residual component (Sumer and Fredsøe, 2002), which is defined by:

$$p_{\mathrm{res}} = \frac{1}{T}\int_{t}^{t+T} p dt \tag{2}$$

where T is the cyclic period of wave loading and t is the time.

Taking into account the soil permeability (k_s), constant in all directions, the conservation of mass for hydraulically isotropic porous seabed (Biot, 1941) can be defined by:

$$k_s\left(\frac{\partial^2 p_{mom}}{\partial x^2}+\frac{\partial^2 p_{mom}}{\partial z^2}\right) - \rho_f g n\beta \frac{\partial p_{mom}}{\partial t} - \rho_f g \frac{\partial}{\partial t}\left(\frac{\partial u_s}{\partial x}+\frac{\partial w_s}{\partial z}\right) = 0 \tag{3}$$

where ρ_f is the pore water density, g is the gravitational acceleration constant, n is the soil porosity, β is the pore fluid compressibility constant, u_s and w_s are the horizontal and vertical displacements respectively.

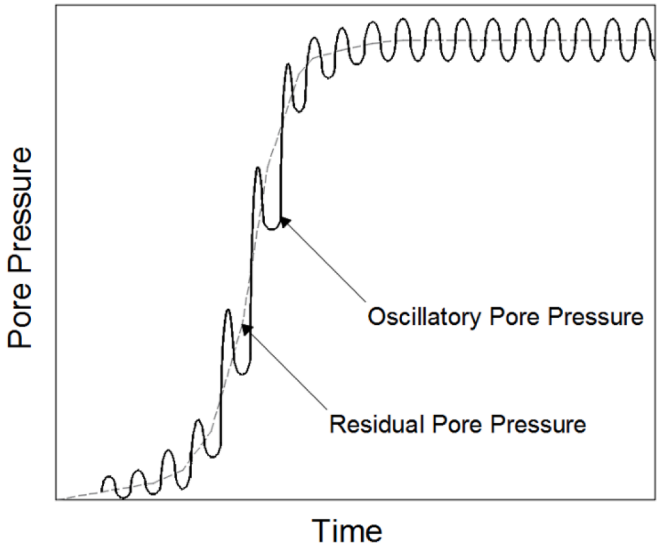

Fig. 2. Wave-induced pore pressure mechanisms in sandy seabed (not in scale).

In the conservation of mass formula, pore fluid compressibility (β) can be written as:

$$\beta = \frac{1}{K_w} + \frac{1-S_r}{p_0} \tag{4}$$

In which K_w is the bulk modulus of water, S_r is the saturation of the seabed soil and p_0 is the absolute pressure (atmospheric + hydrostatic pressure).

Biot's consolidation equations (Biot, 1941) were adopted to simulate the coupling response of pore water within the soil skeleton, while the wave cyclic load was imposed on the surface of seabed. The equilibrium equation for the saturated soil when its domain is considered as a two-phase medium can be expressed by.

$$G\nabla^2 u_s + \frac{G}{1-2\mu}\frac{\partial \varepsilon_V}{\partial x} = \frac{\partial p_{mom}}{\partial x} \tag{5}$$

$$G\nabla^2 w_s + \frac{G}{1-2\mu}\frac{\partial \varepsilon_V}{\partial z} = \frac{\partial p_{mom}}{\partial z} \tag{6}$$

where G is the soil shear modulus, μ is the Poisson ratio. ∇^2 and ε_V are Laplace operator and soil's reversible volume deformation respectively, which can be defined by

$$\nabla^2 = \left(\frac{\partial^2}{\partial r^2}+\frac{1}{r}\frac{\partial}{\partial r}+\frac{\partial^2}{\partial z^2}\right) \tag{7}$$

$$\varepsilon_V = \frac{\partial u}{\partial r}+\frac{u}{r}+\frac{\partial w}{\partial z} \tag{8}$$

For the pore pressure buildup in porous, homogenous soil, the empirical relation and 1D equations were derived from Biot's theory initially (Seed and Rahman, 1978; Sumer and Fredsøe, 2002). The developed equation of pore water accumulation in porous seabed for 2D plain-strain condition (Jeng and Zhao, 2014) can be written as:

$$\frac{\partial p_{\mathrm{res}}}{\partial t} = C_v\left(\frac{\partial^2 p_{\mathrm{res}}}{\partial x^2}+\frac{\partial^2 p_{\mathrm{res}}}{\partial z^2}\right) + f(t) \tag{9}$$

where C_v is the consolidation coefficient in plain strain condition, and $f(t)$ is the source term showing accumulation of pore water as a function of time in sandy seabed (Seed and Rahman, 1978), which can be expressed as:

$$f_{(t)} = \frac{\sigma_0'}{T}\left[\frac{\tau_0}{\alpha_r \sigma_0'}\right]^{1/\beta_r} \tag{10}$$

where σ_0' is the initial mean effective stress, τ_0 is the initial shear stress, α_r and β_r are empirical coefficient, expressed by soil relative density (D_r) as (Sumer and Fredsøe, 2002; De alba et al., 1976):

$$\alpha_r = 0.34 D_r + 0.084 \tag{11}$$

$$\beta_r = -0.37 D_r + 0.46 \tag{12}$$

According to the linear wave theory, when the waves propagate on the surface of sea, the hydrodynamic pressure imposed on the surface of seabed becomes:

$$\mathrm{P_b} = \frac{\gamma_w H/2}{\cosh kd}\cos(kx - \omega t) \tag{13}$$

where $\mathrm{P_b}$ is dynamic wave pressure, γ_w is unit weight of water, H is wave height, k is wave number, d is water depth and ω is wave frequency that may be written as a function of wave number and water depth:

$$\omega^2 = gk\tanh(kd) \tag{14}$$

2.2. Constitutive soil model for sandy seabed

To predict the sequence of wave-induced residual liquefaction in sandy seabed, it is necessary to employ a constitutive soil model capable of considering non-linear stress-strain relationship of sand accompanying the accumulation of pore water pressure under different types of dynamic loads; Therefore, the liquefiable sandy seabed is modelled using CycLiqCPSP, the Elasto-plastic constitutive soil model developed by Wang et al. (2014). Working within the bounding surface plasticity framework (Dafalias, 1986), the constitutive model is able to capture soil response with the aid of formulations for dilatancy of saturated sand in different states (pre to post-liquefaction). The model also has the great advantage of developing shear strains at zero effective stress, and by following dilatancy formulations including reversible and irreversible, it is feasible to link soil's cyclic mobility and dilatancy, which is a significant capability to capture both monotonic and dynamic response of sand. Incorporation of state parameter $\psi = e\text{-}\ e_c$ (i.e., where e is the current void ratio and e_c is the critical void ratio) proposed by Been and Jefferies (1985) makes the model compatible to critical state soil mechanics concept (Fig. 3).

Having adopted a hypoplasticity approach (Wang et al., 1990), plastic loading and load reversal are primarily controlled by:

$$l = \dot{\eta}(\eta - \alpha_{in}) \tag{15}$$

where α_{in} is the stress ratio at the previous load reversal, dictating the plastic loading and reversal occurrence when $l > 0$, and $l < 0$, respectively.

The incremental stress-strain relationships are consistent with those of classic elasto-plasticity:

$$\dot{\varepsilon}_q^e = \frac{\dot{q}}{3G}; \quad \dot{\varepsilon}_v^e = \frac{\dot{p}}{K}; \quad \dot{\varepsilon}_q^p = \frac{\dot{\eta}}{H}; \quad \dot{\varepsilon}_v^p = D\left|\dot{\varepsilon}_q^p\right| \tag{16}$$

where the superscripts e and p refer to the elastic and plastic strains. Elastic shear modulus, plastic shear modulus and dilatancy rate are denoted by G, K, H and D, respectively. The peak mobilized stress ratio, has been defined in accordance with an exponential variation with Ψ as proposed by Li and Dafalias (2000):

$$M_p = Mexp\left(-n^b\Psi\right) \tag{17}$$

The plastic modulus representing the bounding surface plasticity theory was suggested as:

$$H = \frac{h}{p}Gexp(-n^p\Psi)\left(\frac{Mexp(-n^p\Psi)}{M_m}\left(\frac{\overline{\rho}}{\rho}\right) - 1\right) \tag{18}$$

With ρ being the distance between the current stress ratio η to α_{in} and $\overline{\rho}$ is the distance between the projection of current stress on the maximum stress ratio surface and α_{in}.

CycLiqCPSP constitutive soil model consists of 15 parameters, where G_0 and κ = elastic modulus constants, h = plastic modulus parameter, M, λ_c, e_0 and ξ = critical state parameters, n^p, n^d = state parameter constants, $d_{re,1}$, $d_{re,2}$ = reversible dilatancy parameters, and d_{ir}, α, $\gamma_{d,r}$ = irreversible dilatancy parameters.

The constitutive soil model has previously been validated by simulating undrained torsional tests, undrained and drained triaxial tests, centrifuge model tests and showed successful results, in particular when it was used for the purpose of SFI problems in liquefiable soils (Wang et al., 2016; Wang and Zhang, 2018).

3. Wave-induced liquefaction in seabed

OpenSees showed great capability of simulating SFI problems in offshore environment (Barari et al., 2017a; 2021b). Wang and Zhang (2016) indicated the feasibility of OpenSees for wave-seabed interaction problems in poro-elastic seabed. Later, Wang and Zhang (2018) verified adequacies of CycLiqCPSP constitutive soil model against wave-seabed-pipeline interaction in poro-elasto-plastic seabed.

In this section, parameters of the constitutive soil model were validated in two subsequent stages. First, the element testing was conducted with the aid of the numerical simulation of cyclic simple shear (CSS) test to calibrate the parameters of the constitutive soil model. Element test allows one to evaluate the liquefaction parameters of non-cohesive soils under cyclic loading. Secondly, parameters of the CycLiqCPSP constitutive soil model were validated by simulating the centrifuge test to examine the wave-induced seabed liquefaction problem in OpenSees, allowing authors to examine soil response in condition equal to stresses in prototype.

3.1. Calibration of soil model parameters

The CSS tests results for given Leighton buzzard sand were not available in literature, therefore, experimental results of a group of sands with gradation characteristics relatively similar to those of Leighton buzzard sand were selected to carry out the calibration phase.

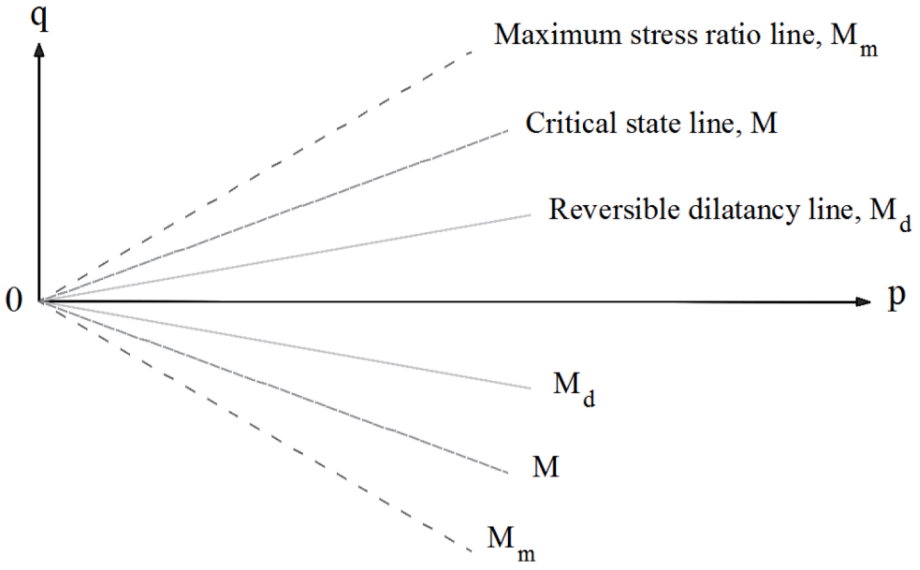

Fig. 3. Schematic illustration of critical state soil mechanics concept.

CSS tests data available on the selected sands with different relative densities (D_r), overburden stresses (σ'_{v0}) and cyclic stress ratios (CSR $= \tau/\sigma'_{v0}$) were used for the calibration. More details about the CSS tests of the selected sands, including: Nevada sand, Monterey sand, Ottawa sand (A), Sacramento river sand, Ottawa sand (B) and Fuji river sand are available in Arulmoli et al. (1992), Kammerer et al. (2004), Bastidas (2016), Boulanger and Seed (1995), Ziotopoulou et al. (2018) and Ishihara and Yamakazi (1980), respectively. Table 1 summarizes the calibrated parameters of CycLiqCPSP constitutive soil model. The relation between CSR and the number of cycles leading to onset of liquefaction (single amplitude shear strain of 3%) is compared in Fig. 4, based on the output results obtained from the numerical CSS simulations carried out in OpenSees and the available experimental CSS tests on the selected sands. Since the constitutive model was developed to capture sand at any relative density using the same set of parameters and merely varying the initial void ratio, the validation exercise shows that this set of parameters to be appropriate for loose, medium dense and dense sand ($D_r = 40\%$, 60% and 80%) with initial void ratios of $e_{in} =$ 0.88, 0.8 and 0.72, respectively.

3.2. Predictions for wave-induced liquefaction of seabed in a centrifuge facility

The process of calibration and prediction using CycLiqCPSP model was iterative with the first stage informing the second stage while predicting the liquefaction of seabed induced by wave action. The centrifuge facilities data from Sassa and Sekiguchi (1999) were employed to gain a better insight into the capability of FE numerical model in simulating the process of pore pressure accumulation within a level ground seabed under the action of waves (partial drainage condition) until the liquefaction stage. Fig. 5 shows the experimental setup for the centrifuge experiments in which a wave paddle is responsible for the generation of progressive waves and the subsequent accumulated pore pressure in the sand.

Test P5-1 among all other tests was chosen for the sake of calibration in this study. The predictions were carried out in prototype scale; hence, according to the scaling principle, a sand container (10 m × 5 m) consisting of 800 Quadrilateral Four-Node-Quad-u-p elements is considered to simulate the centrifuge test in FE framework. As shown in Fig. 6, the wave pressure was calculated using Eq. (13) and was applied on the seabed grid points as nodal hydrodynamic forces, causing shear stresses on the soil elements; consequently, leading to shear-induced deformations and pore pressure buildup within the soil domain. Fully-fixed-displacements bottom, horizontally-fixed lateral boundaries and free-displacement upper boundary were set for the sand container model. It should be noted that the bottom and the two lateral boundaries are defined as impervious, while the upper boundary is permeable to capture the wave pressure imposed on the surface as nodal forces. Details of boundary conditions, damping, and wave pressure exertion are

Table 1
Parameters of CycLiqCPSP constitutive soil model in calibration phase.

Parameters	Value
Parameter of elastic shear modulus, G_0	70
Parameter of Elastic bulk modulus, κ	0. 006
Plastic modulus parameter, h	1.2
Critical state stress ratio, M	1.25
Reversible dilatancy, $d_{re,1}$	0.01
Reversible dilatancy, $d_{re,2}$	10
Reference shear strain, $\gamma_{d,r}$	0.05
Irreversible dilatancy ratio, α	30
Irreversible dilatancy potential, d_{ir}	0.65
Critical state constant, λ_c	0.019
Critical state constant, ξ	0.7
Void ratio at $p_c = 0$, e_0	1. 13
State parameter constant, n^p	1.1
State parameter constant, n^d	7.8

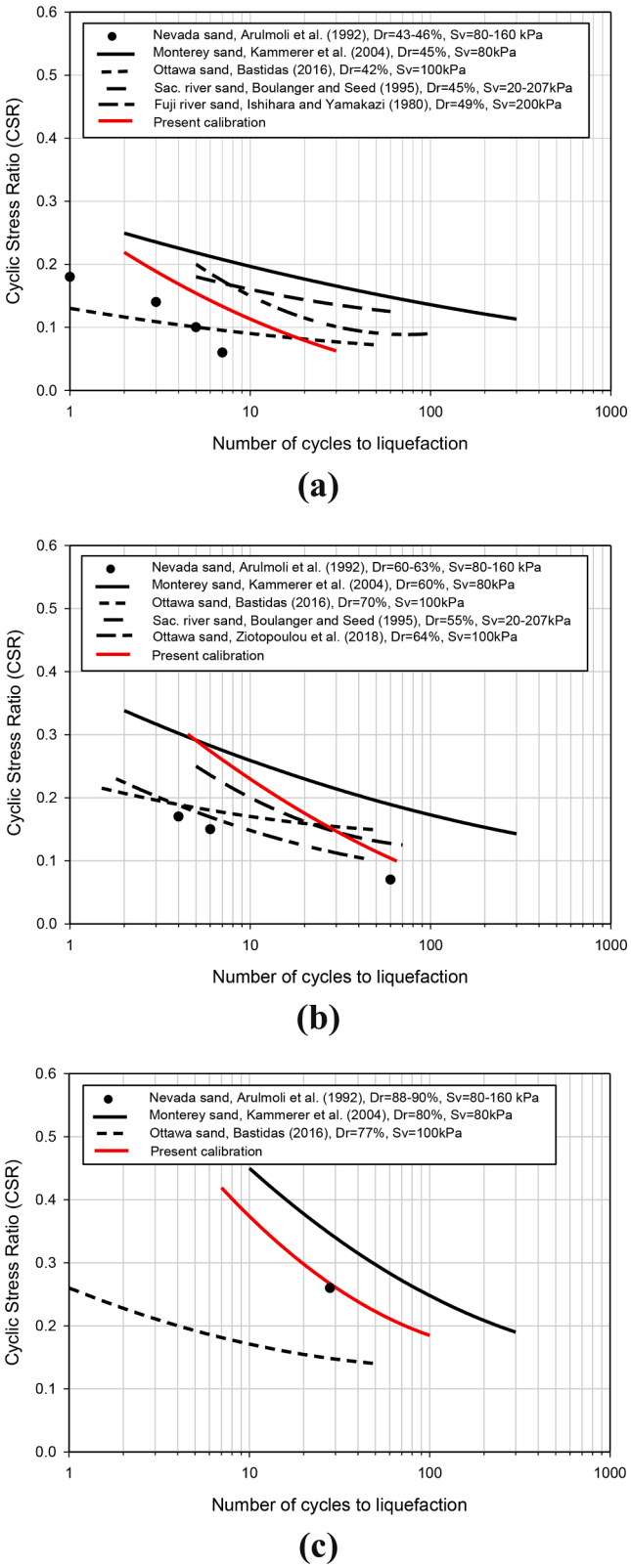

Fig. 4. Relation between CSR and the number of cycles required for the onset of liquefaction (single amplitude shear strain of 3%) in the available experimental CSS test on the selected sands with the numerical simulations performed in OpenSees.

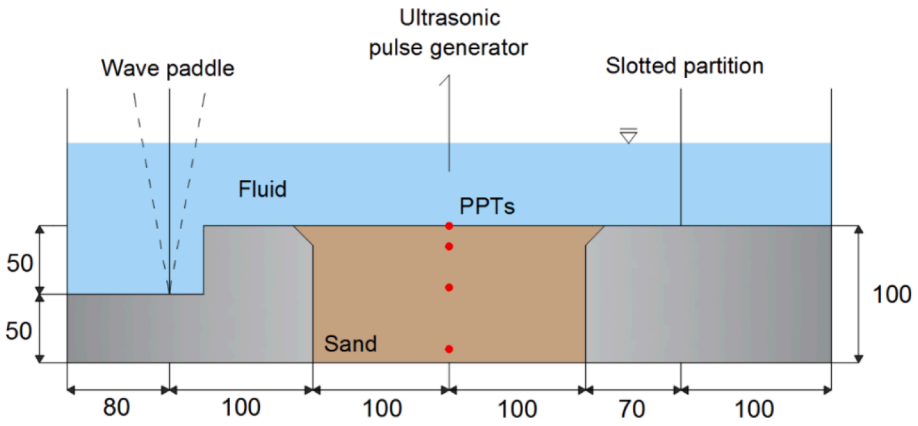

Fig. 5. Wave tank used by Sassa and Sekiguchi (1999) for centrifuge test (dimensions in mm).

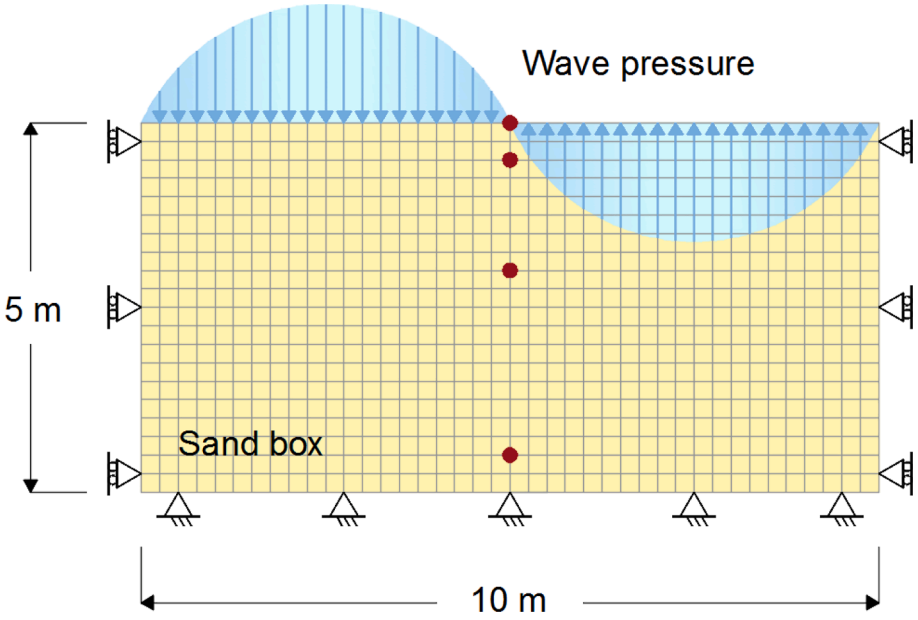

Fig. 6. Numerical Scheme of centrifuge test.

given in the next section (section 4), primarily due to the similarities in the processes. Parameters of constitutive soil model are listed in Table 1 (D_r = 40%), and wave characteristics as well as advanced soil parameters are tabulated in Table 2. Four monitoring points at the centerline of sand container were chosen (0 m, 0.5 m, 2 m & 4.5 m) to measure the pore pressure response. Fig. 7 illustrates the numerical predictions of excess pore water pressure development over the interval wave passes through the sand along with experimental data. It could be observed that there is a reasonable agreement between the numerical model and experimental observation in Sassa and Sekiguchi (1999).

Table 2
Wave characteristics and soil properties used in model test in centrifuge facility.

Parameters	Value
Wave characteristics	
Wave period, T (s)	4.5
Wave height, H (m)	1.6
Wavelength, L (m)	10
Water depth, d (m)	4.5
Soil properties	
Density of soil, ρ_s (kg/m^3)	1860
Permeability of soil, k_s (m/s)	1e-5
Density of pore water, ρ_w (kg/m^3)	1000
Bulk modulus of water, B_f (Pa)	2.2e9

4. Numerical setup

4.1. Numerical method

In order to simulate the wave-induced liquefaction around a caisson-supported offshore wind turbine, plane-strain analysis was performed using the FEM framework, OpenSees. The algorithm adopted for this study is illustrated in Fig. 8. Based on Biot's theory for porous medium (Biot 1941) and the u-p formulation for the low-frequency dynamics of water-saturated soil (Zienkiewicz et al., 1980; Zienkiewicz and Shiomi, 1984), the simulation domain was constructed with the aid of Quadrilateral Four-Node-Quad-u-p solid-fluid coupled element which has three degrees of freedom (two for displacements and one for pore pressure) at each node (Yang et al., 2008). As the geotechnical aspects of the wave-seabed-foundation interaction was the main goal of this work and not the structural response of the steel caisson, Four-Node-Quad element with two displacement degrees of freedom was used to create the caisson

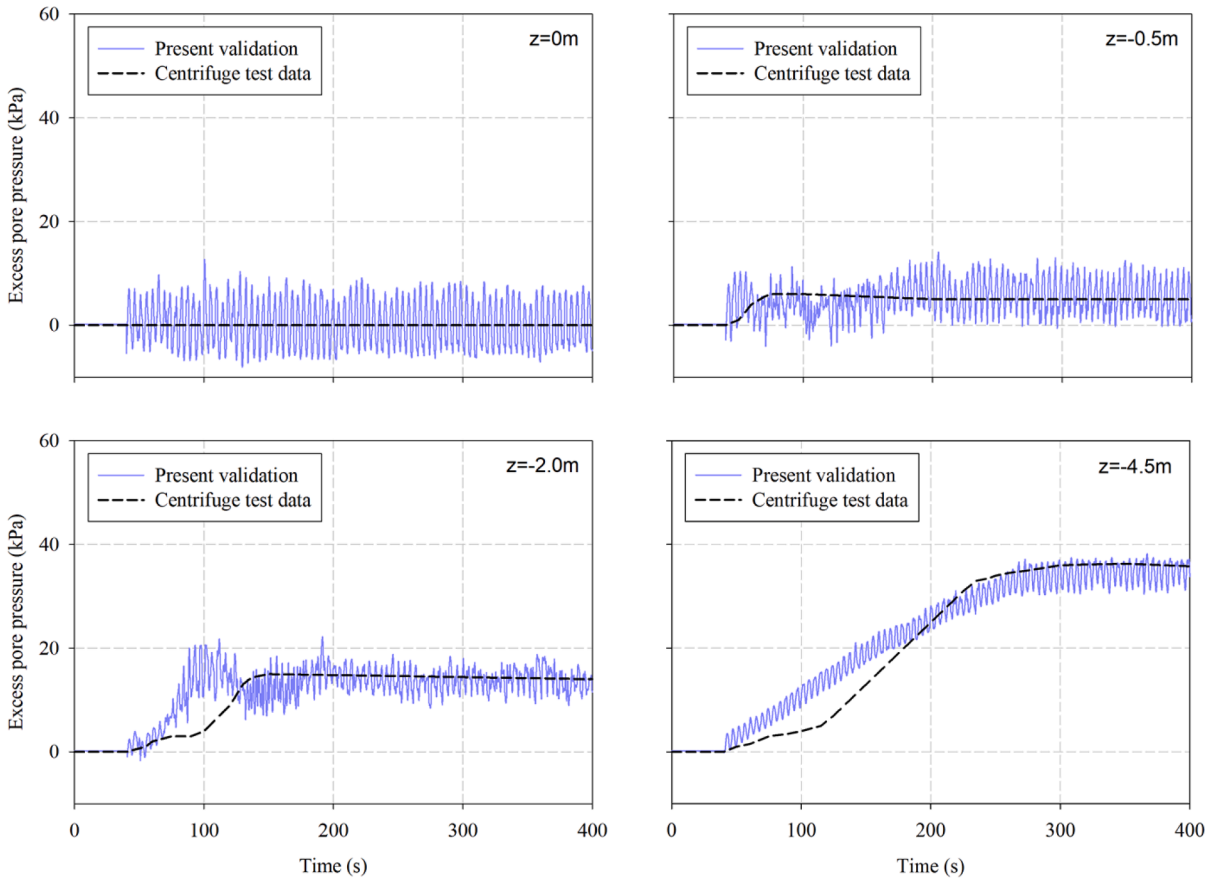

Fig. 7. Comparisons of the results between simulated results and experimental data conducted by Sassa and Sekiguchi (1999).

domain.

Moreover, the CycLiqCPSP Elasto-plastic constitutive model was employed to establish the sandy seabed.

The caisson foundation, consisting of lid and skirt, acts as an integrated unit within the seabed soil. Due to the fact that the caisson is generally made of steel, it is treated as an impervious material by setting its permeability very low (1e-20 m/s). Constitutive model of Elastic-isotropic material was adopted for construction of the foundation's domain. Table 3 provides the parameters for the finite-element numerical simulations. In addition, Parameters of CycLiqCPSP constitutive soil model for the liquefiable ($D_r = 40\%$) and the non-liquefiable ($D_r = 80\%$) soil are listed in Table 1.

In this study, thickness of the lid was assumed thinner than the convention due to the limitation of using triangular elements in OpenSees, and the thickness of the skirt was assumed thicker than the real condition in order to prevent the discontinuity in meshing system leading to divergence of numerical analysis (Esfeh and Kaynia, 2020). Consequently, modifications were performed on different sections (lid or skirt) based on the equilibrium of total mass ($\rho_{eq}A_{eq} = \rho_{sec}A_{sec}$) and equilibrium of total stiffness ($E_{eq}I_{eq} = E_{sec}I_{sec}$) separately, where ρ, A, E and I are unit mass, area, elastic modulus and moment of inertia respectively as suggested in Barari et al. (2017a, 2021b). The subscripts *eq* and *sec* stand for the equivalent (modified) value and the desired section (lid or skirt), respectively. Eventually, equivalent unit mass of the lid and the skirt are 4 times greater than and 0.1 of the values in Table 3 respectively, and equivalent elastic modulus of the lid and the skirt are 12 times greater than and 0.1 of the values in Table 3 respectively.

Total mass of the OWT placed on the foundation was taken into account according to a standard 5-MW offshore wind turbine (Jonkman et al., 2009). This is a reference model defined by National Renewable Energy Laboratory (NREL) for researchers. OWT tower was modelled as a rectangular (3 m × 80 m) structure using Quad elements (0.5 m × 10 m) and Elastic-isotropic material. Tower's mass was distributed on its body as a modified specific density (ρ_t). Moreover, the sum of rotor and nacelle was applied at top center of the tower as a nodal mass.

Fig. 9 depicts the FE model created for plane-strain analyses; the discretized model area consisted of approximately 1400 elements and 1500 nodes to model the soil medium. A convergence study had also been conducted to determine the sufficient domain size and mesh fineness (Moghaddam et al., 2020). The configuration was discretized into quad structured mesh with an element size of 1 m × 1 m, while for the caisson and the soil in the vicinity of foundation area, finer mesh with element size of 0.5 m × 1 m was used. Although it is recommended to consider a seabed domain 2–3 times longer than wave-length in computational fluid dynamics (CFD) examinations due to the real-mode simulation of waves, in the current study, a seabed domain approximately 5 times longer than the caisson diameter was found to be appropriate because of the new approach adopted for the implementation of waves' calculated nodal forces acting on the seabed surface grids. The need for assigning absorbing side boundaries to reduce edge reflections and seepage was revisited but results were not affected.

A fully bonded soil-foundation interface with no links was considered in numerical model (Barari et al., 2017a, 2021b). Incorporating a fine mesh in seabed domain, not only facilitate the proper exertion of wave loading on the seabed surface, but also let the loss of soil's strength occur during the liquefaction, control the nonlinearity at the soil-foundation interface. The size of the soil elements at the interface zone varies from 2.7% to 5% of the size of caisson's diameter.

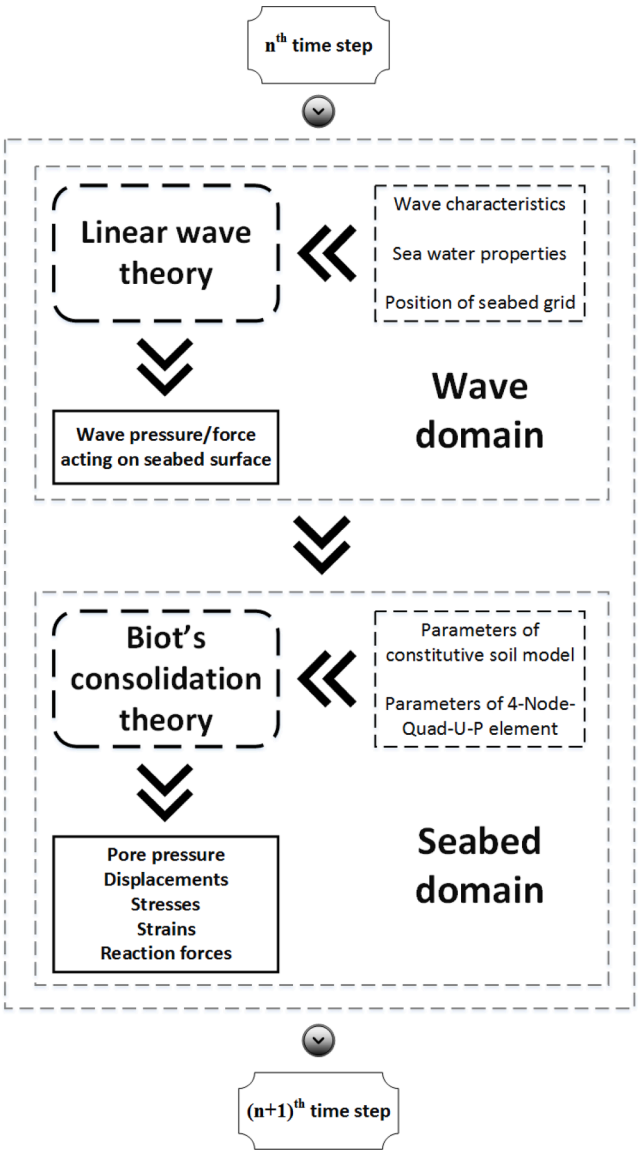

Fig. 8. Algorithm adopted for the wave-seabed-foundation interaction in OpenSees.

4.2. Solution procedure

A time-domain numerical solution was employed for a dynamic equilibrium formulation of the total soil-foundation system as follows:

$$M\ddot{U} + CU + K\dot{U} = R(t) \tag{19}$$

where $\ddot{U}, \dot{U}$ and U are relative nodal acceleration, velocity, and displacement values, respectively. Meanwhile, *M*, *C*, and *K* represent mass, damping, and stiffness matrices, respectively, and *R(t)* is a time-varying external load. Material damping was considered to be hysteretic in nature and encompassed by an elasto-plastic soil model. Furthermore, effects from both material damping and radiation damping are addressed by [C], a global damping matrix.

By neglecting the relative velocity of the fluid phase in a fully coupled analysis, the FE governing equations in a u-p formulation are as follows:

$$M\ddot{U} + \int B^T \sigma' dV - QP - f^{(s)} = 0$$

Table 3
Parameters of the WSFI model in the present study.

Parameters	Value
Wave characteristics	
Wave period, T (s)	7
Wave height, H (m)	4
Wavelength, L (m)	47.5
Water depth, d (m)	15
Seabed properties	
Seabed domain length, L_d (m)	74
Seabed domain height, h (m)	15
Thickness of liquefiable layer, $t_{s,l}$ (m)	3, 7, 11, 15
Density of liquefiable soil, $\rho_{s,l}$ (kg/m^3)	1700, 1800, 1900
Density of non-liquefiable soil, $\rho_{s,n}$ (kg/m^3)	2100
Permeability of liquefiable soil, $k_{s,l}$ (m/s)	1.7e-4
Permeability of non-liquefiable soil, $k_{s,n}$ (m/s)	4e-5
Density of pore water, ρ_w (kg/m^3)	1000
Bulk modulus of water, B_f (Pa)	2.2e9
Foundation properties	
Density of steel (caisson), ρ_c (kg/m^3)	7850
Permeability of foundation, k_f (m/s)	1e-20
Elastic modulus of foundation, E_f (Pa)	2e11
Poison's ratio,υ	0.3
Caisson diameter, D_c (m)	10, 14
Lid thickness, t_l (m)	0.4
Skirt length, L_s (m)	4, 7, 10, 13
Skirt thickness, t_s (m)	0.5
Offshore wind turbine properties	
Tower mass (kg)	347e3
Nacelle mass (kg)	240e3
Rotor mass (kg)	110e3
Elastic modulus of foundation, E_t (Pa)	2e11
Density of steel (tower), ρ_t (kg/m^3)	1446

$$Q^T\dot{U} + HP + S\dot{P} - f^{(p)} = 0 \tag{20}$$

where *M*, *B*, and σ' denote the mass matrix, strain-displacement matrix, and effective stress vector, respectively; *Q* holds for the discrete gradient operator coupling the solid and fluid phases; *P* is the pore water pressure vector; *H* is the permeability matrix; and *S* is the compressibility matrix. Furthermore, the effects arising from body forces and the boundary conditions for both solid and fluid phases are described by $f^{(s)}$ and $f^{(p)}$, respectively.

For the gravitational analysis, the seabed soil model without the foundation was modelled and assigned elastic properties initially. Permeability of whole domain was set artificially very large (1 m/s) to facilitate consolidation while the self-weight of soil was considered in this step. Subsequently, the soil behaviour was tuned as plastic material and the permeability of each domain was updated to its desired value. Next, the seabed soil was replaced by caisson foundation material followed by a relief analysis to obtain the initial effective stress considering soil and foundation self-weight and gravity loading.

For the dynamic analysis, the wave pressure was imposed on the seabed surface as time-varying nodal load using the Sine time series and Plain Pattern command, while Newmark method was used as time integrator scheme. In line with soil permeability, soil density, loading amplitude, etc., the numerical simulations showed that a time step of $dt = 0.01$ s is required to proper exertion of waves' calculated nodal forces acting on the seabed surface. ProfileSPD approach along with the Krylov Newton solution algorithm was adopted to solve the system of equations. Rayleigh damping was included in the soil-structure model created. In addition, the mass (α) and stiffness (β) coefficients were 0.502 and 0.003, respectively; and these resulted in a minimum

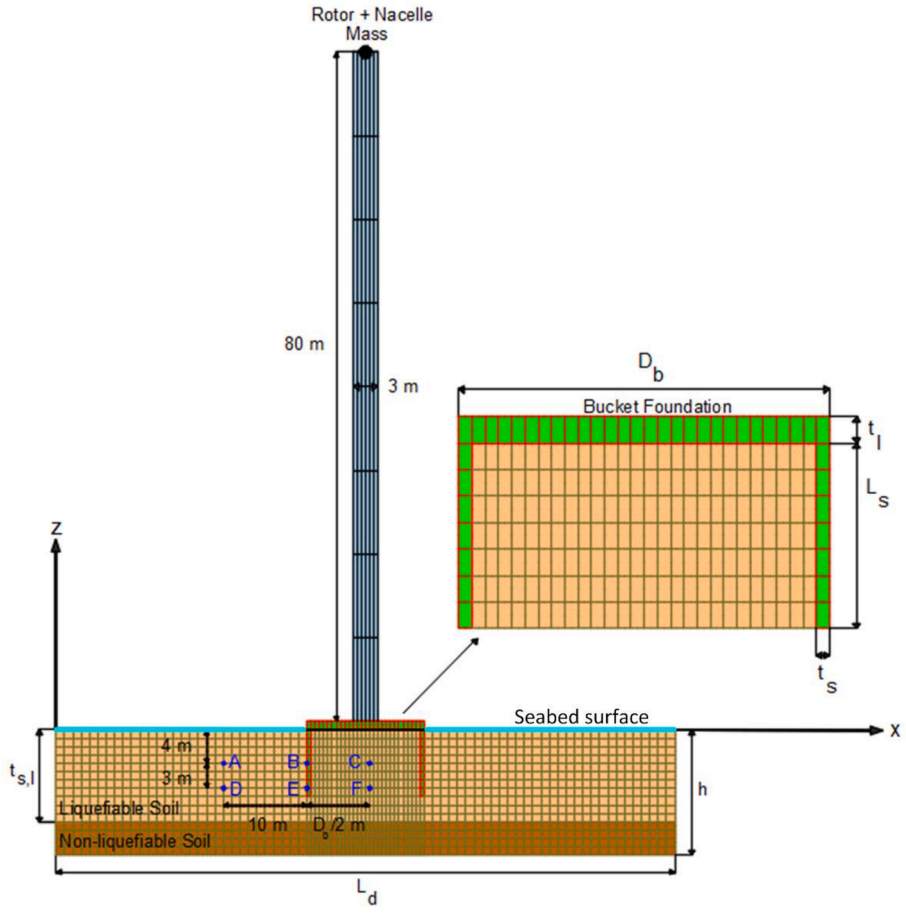

Fig. 9. Computational domain of wave-seabed-foundation interaction in FEM.

damping ratio of 5% which is consistent with high period wave components (T = 7 s).

The mesh discretization, time steps and model solver were optimized through sensitivity analyses. Analyses are performed with the aid of the high performance computing facility (HPCaaS) in order to reduce the running time of each simulation.

4.3. Boundary conditions

The appropriate boundary conditions are essential for the examination of the wave-induced liquefaction around offshore foundations. The following boundary conditions were applied for the numerical calculation:

(1) At the seabed surface, the pore water pressure was equal to dynamic pressure imposed on the seabed surface and the vertical effective stress and shear stress were assumed to be zero.

$$P = P_b \ and \ \sigma'_{zz} = \tau_{xz} = 0 \ at \ z = 0 \tag{21}$$

where σ'_{xx} = vertical effective stress, τ_{xz} = shear stress.

(2) At the two sides of the model, appropriate boundary was adopted by constraining the nodes at equal depths to have the same displacements in horizontal direction with the aid of EqualDOF command in OpenSees. Boundaries were considered to be impervious, without any horizontal displacements.

$$\frac{\partial P}{\partial x} = 0, u_x = 0 \ \text{at} \ x = 0 \ \text{and} \ x = L_d \tag{22}$$

In which u_x is horizontal displacement.

(3) A rigid, impermeable boundary was taken into account for the bottom of the seabed; thus, displacements in all directions were fixed and vertical flow is prevented.

$$u_x = u_z = 0 \ \text{and} \ \frac{\partial P}{\partial z} = 0 \ \text{at} \ z = -h \tag{23}$$

In which u_z is horizontal displacement.

(4) Suction caisson foundation was considered to act as an impermeable boundary in computation. The displacements of foundation in all directions were set to be free to take into account the effect of initial stresses which were generated during the consolidation analysis.

$$\frac{\partial P}{\partial n} = 0 \tag{24}$$

where *n* is the perpendicular direction to the caisson segments' surfaces.

5. Results and discussions

5.1. Wave-induced liquefaction around caisson foundation.

The accumulative compression of the seabed soil under waves' vertical pressure results in the development of excess pore pressure. When the excess pore pressure reaches the level of initial effective vertical stress, the seabed soil loses its shear strength; consequently, failing to support offshore foundation.

The proposed criterion for identifying the residual wave-induced liquefaction in plain-strain condition is:

$$r_u = \frac{\Delta u}{\sigma'_{v0}} \tag{25}$$

where r_u is the excess pore pressure ratio, Δu is the excess pore pressure and σ'_{v0} is the initial vertical effective stress. Liquefaction was assumed to trigger when the $r_u = 0.9$ is exceeded. In order to gain insight into the process of residual wave-induced liquefaction in the vicinity of caisson foundation, two rows of points each including three points were selected as demonstrated in Fig. 9. Monitoring point rows were located 4 m and 7 m below the mudline. Points A and D were located 10 m away from the foundation which were assumed to represent the free-field response, once a comparison with free-field is of interest. Points B and E were located next to the skirt to scrutinize the WSFI problem rigorously. Points C and F were located in the soil within the foundation to evaluate the complicated response of soil in this region. The thickness of the liquefiable layer ($t_{s,l}$) was 11 m and the suction caisson foundation with parameters $D_b = 14$ m and $L_s = 7$ m (embedment ratio = 0.5) served as purpose benchmark model throughout this section.

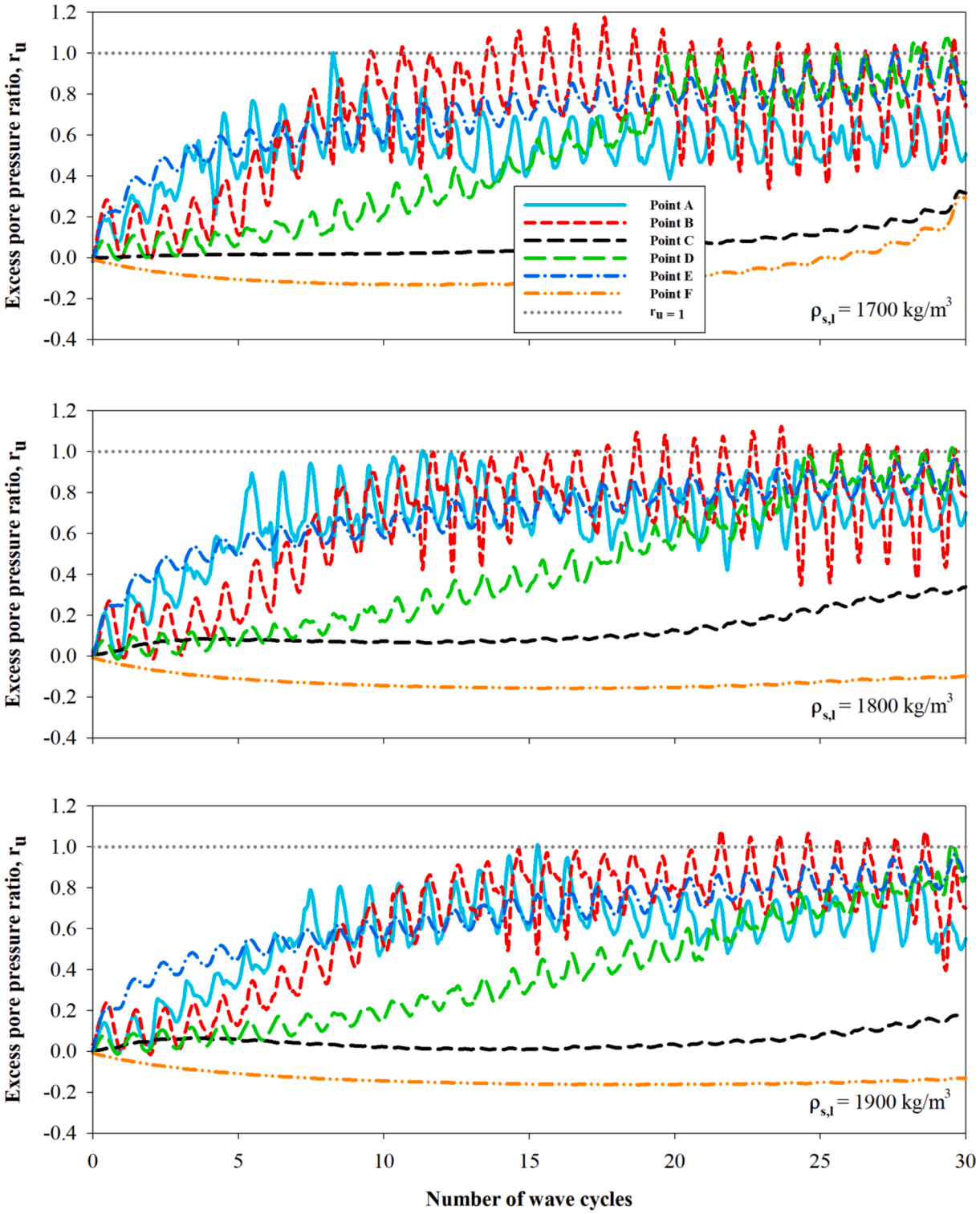

Fig. 10. Excess pore pressure buildup at monitoring points for various specific densities.

Fig. 10 presents the development of r_u at different locations for various specific densities of the liquefiable sandy seabed ($\rho_{s,l}$ = 1700, 1800 and 1900 kg/m^3). It can be seen that greater tendency of lower density sand to compress led to faster net excess pore pressure buildup. This also amplified the settlement mechanism of foundation as discussed in section 5.3 more comprehensively. Seabed soil at monitoring points A and B liquefied faster than other points due to the lower vertical effective stress in this depth and more intense impact of the wave-induced dynamic forces on the seabed surface as well. It is also observed that the effect of the presence of structure and its wave-induced rocking vibration on the onset of liquefaction is negligible or marginal if any (Miyamoto et al., 2020). Conversely, for the initiation of liquefaction around point C, more cycles of wave loading was required due to the higher vertical effective stress in this region caused by the presence of heavy OWT on the foundation. Furthermore, as monitoring point C was not under the direct impact of wave loading, shear stresses barely affected the soil in these areas; therefore, the fluctuation of pore pressure and its subsequent accumulation was considerably low in comparison to points A and B which were directly affected by the wave-induced forces.

After 30 cycles of wave loading, seabed soil at monitoring points D and E exhibited a lower tendency to liquefy, however, it appears that for deeper layers, more cycles of wave loading was yet required for the full liquefaction. This late liquefied time interval in deeper zones did not only stem from the higher vertical effective stress, but also for the weaker impact of waves' cyclic forces. The faster development of EPWP at point E in comparison to point D is mainly caused by the presence of the caisson foundation. The SSI-induced deviatoric mechanism due to the wave-induced cyclic forces on the skirt and at the tip amplifies the PWP development in this region compared to point D at free-field.

Monitoring point F within the skirt, experienced a negative excess pore pressure initially due to the dilative tendency of sandy soil in this region; however, the excess pore pressure rose gradually due to the seepage from the lower layers caused by generation of hydraulic gradients (Karimi et al., 2018). Rather interestingly, the longer drainage path may have been the reason for a late time interval where negative EPWP turns in to softening effect.

Also, EPWP distribution of FE domain around the caisson is demonstrated in Fig. 11. As it is revealed in the plots, at the beginning of wave loading, no EPWP can be observed. However, at the 10th cycle, EPWP build-up appears adjacent to the skirt tips and at the depth of 4 m below the seabed surface. In the following, at the 20th cycle, the EPWP development at the aforementioned regions becomes more significant besides the slight EPWP generation within the caisson. Finally, contour plots of 30th cycle demonstrate the highest amount of EPWP build-up below the skirt tips and also within the caisson and at the depth of 7 m below the seabed surface.

5.2. *Wave-induced EPWP and initial stress distribution.*

Stress path of sandy seabed under the action of cyclic wave loading at the monitoring points for various specific densities ($\rho_{s,l}$ = 1700, 1800 and 1900 kg/m^3) are compared in Figs. 12 to 14, respectively. Two different phases are indicated in the plots to display the soil response during the cyclic loading. Pre-liquefaction phase shows the hysteretic response of sand (blue segments), while post-liquefaction phase depicts the yielding response after the onset of liquefaction (red segments). As can be seen in Fig. 12, for lower specific density ($\rho_{s,l}$ = 1700 kg/m^3), stress paths of points A and B (z = -4 m) clearly show that after some symmetric loops during the pre-liquefaction phase, soil goes into the post-liquefaction phase by loss of shear strength, but with a higher deviatoric stress at point B due to the presence of initial shear stresses adjacent to the foundation. The presence of static shear stress also resulted in a reduction of the cyclic resistance of the sand adjacent to the caisson moving it faster to the failure envelope. The consistency is literally apparent with Castro and Poulos (1977). The apparently contradictory result was obtained within the caisson where an abrupt drop of effective stress due to the generation of PWP build-up was followed by the dilative behavior of sand which led to decrease of PWP and rapid increase of effective stress. However, the increase was negligible because it compensated for the loss of effective stress occurring at the

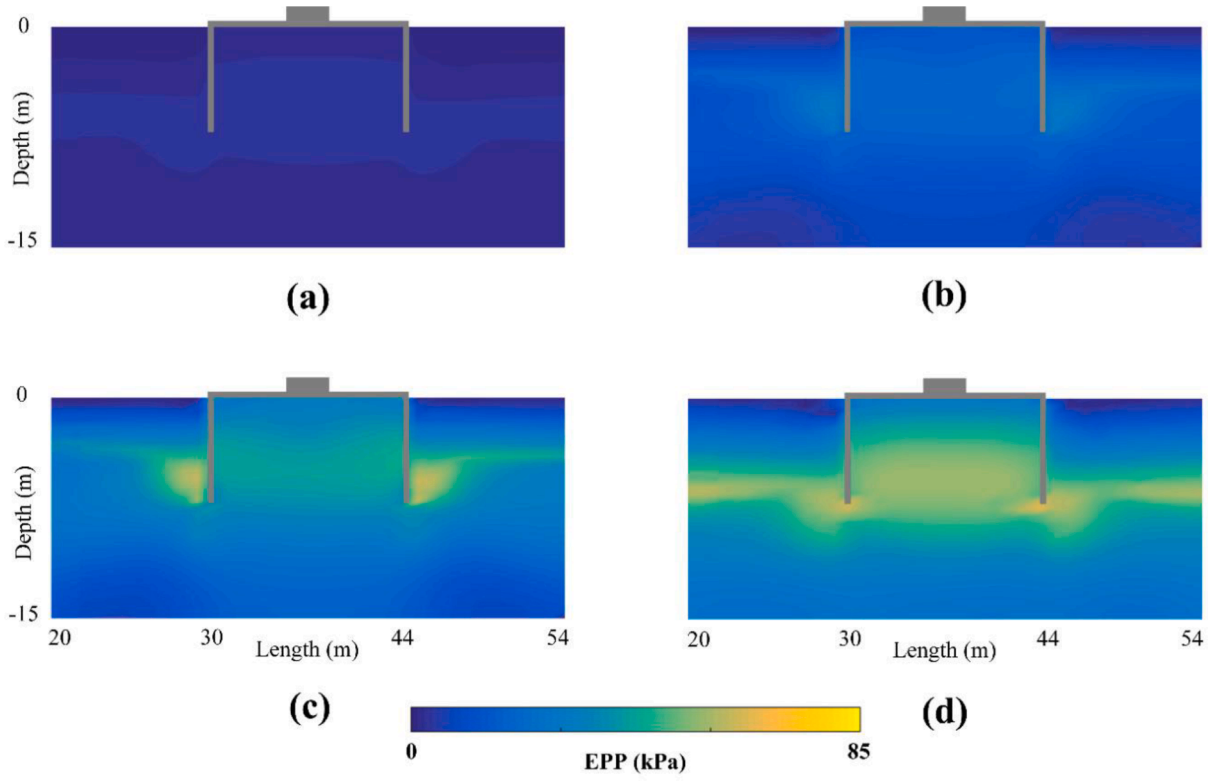

Fig. 11. Contour plots of EPWP distribution around the caisson for four different time instants: a) 0th, b) 10th, c) 20th and d) 30th cycle of wave loading.

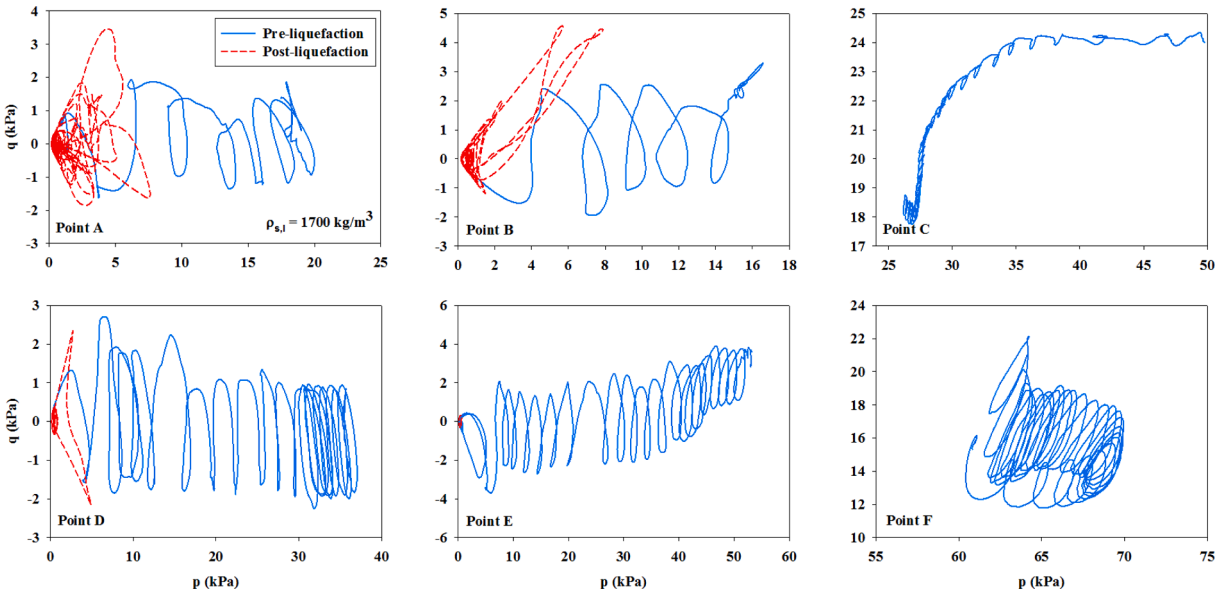

Fig. 12. Stress path of monitoring points for $\rho_{s,l} = 1700$ kg/m^3.

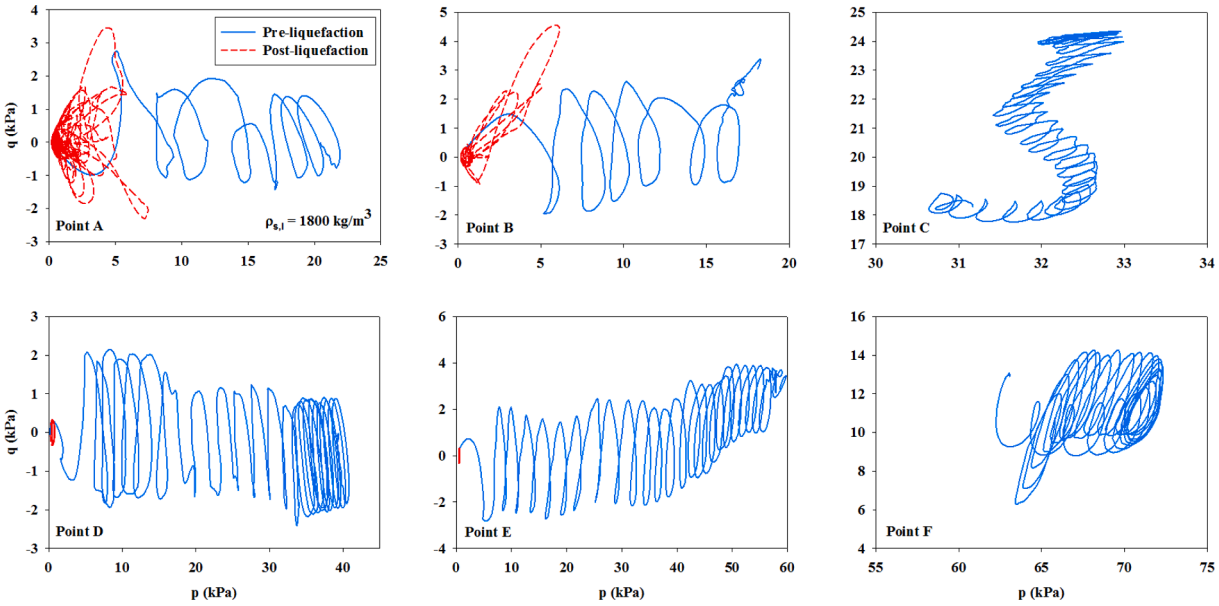

Fig. 13. Stress path of monitoring points for $\rho_{s,l} = 1800$ kg/m^3.

next step due to the hydraulic gradient and the subsequent pore pressure accumulation. An increase in contact pressure at points D and E (z = -7 m) resulted in increase in soil's strength and resistance to pore pressure generation and liquefaction; nevertheless, the wave action was strong enough to overcome the higher resistance despite more cycles of wave loading was required for the initiation of fully-liquefied stage. Similar to the scenario occurring at point C, stress path of point F at tip level demonstrates the dilative behavior of sand and the following hydraulic gradients lead to successive increase and decrease of effective stress at this region, respectively during the 30 cycles of wave loading. Plots in Fig. 13 reveal that the same process occurred for all monitoring points except for point D, which only liquefied momentarily due to its higher specific density of sand ($\rho_{s,l} = 1800\,\mathrm{kg/m^3}$), stiffness and resistance to softening in spite of initial state variables considered (confining stress, relative density). Also it is evident that for monitoring point C, increase of effective stress caused by the dilative behaviour of sand was more pronounced, primarily due to the higher density of sand.

Although the stress path trends for all monitoring points in Fig. 14 are similar to those in Fig. 13, the mutual interplay of initial state variables (static shear, confining stress, relative density) in controlling the cyclic behaviour of saturated sand is rather obvious.

Comparison between stress paths in Figs. 13 and 14 show that the observed reduction in the generated excess pore pressure and softening capability below the foundation edge (point E versus point D) corresponds well with the areas characterised by high value of static shear stress ratio (α). These contradictory results with findings reported by Castro & Poulos (1977) and Seed & Harder (1990) were scrutinised by Vaid and Chern (1983) and Vaid et al. (2001) who attributed this controversial influence of static shear stress to its strong dependency on two other variables. Here, the cyclic shear stresses (τ_{cyc}) applied was slightly higher than initial shear stress (τ_i), therefore a partial stress-reversal mechanism yet took place, roughly increasing its cyclic resistance, in accordance with similar studies using element testing (Harder & Boulanger, 1997) despite significant differences between the loading

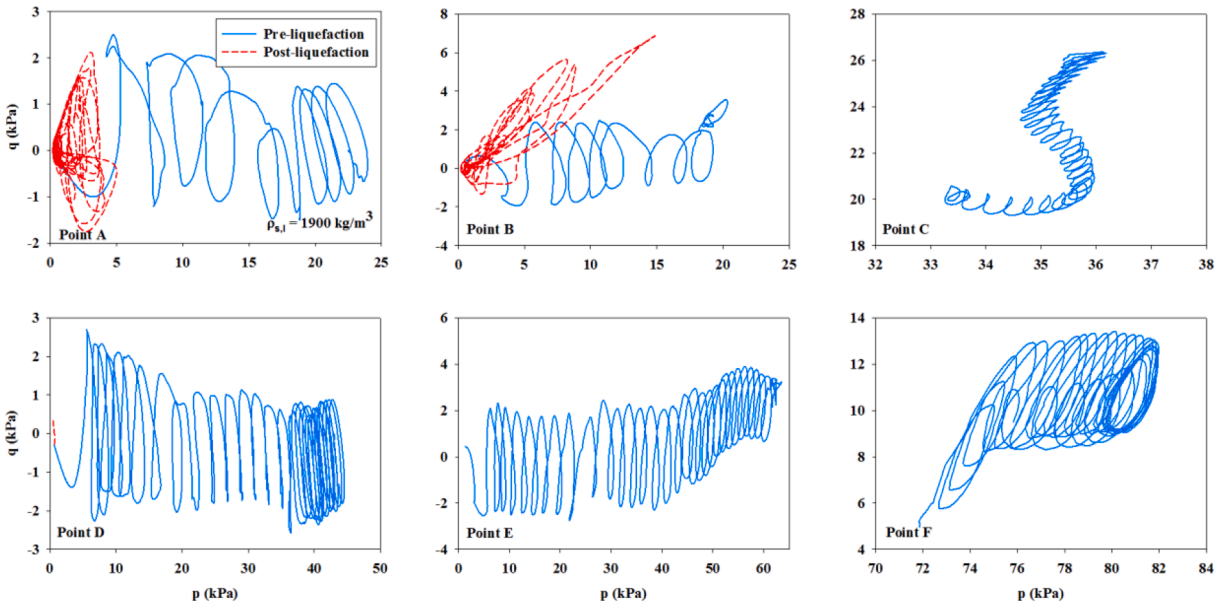

Fig. 14. Stress path of monitoring points for $\rho_{s,l} = 1900$ kg/m^3.

type, drainage and boundary conditions of an element test and those in an offshore soil-structure interaction problem. In the FE simulations performed, the presence of caisson-induced static shear stress at point E with the $\sigma'_v \sim 60kPa$, the increased cyclic resistance was observed, which is in comply with the static shear stress-induced correction factor for liquefaction resistance K_α curves proposed by Vaid et al. (2001) for relative density $D_r = 55-70\%$ and $\sigma'_v \sim 100kPa$ (Fig. 14).

5.3. Liquefaction-induced OWT settlement.

In this section, influence of seabed characteristics (specific density of liquefiable layer and seabed stratification), caisson foundation properties (skirt length and foundation diameter) and OWT weight on the mechanisms contributing to the settlement of foundation were assessed.

(a) Influence of thickness of liquefiable layer

Fig. 15 shows the varying seabed stratification where the thickness of the seabed soil (h) is 15 m, skirt length (L_s) is 7 m with four different thicknesses of liquefiable layer, ($t_{s,l}$) (3 m, 7 m, 11 m and 15 m) to evaluate the influence of the liquefiable crust layer thickness on the settlement of foundation after 30 cycles of wave loading. Although in the first condition with $t_{s,l} = 4$ m, skirt's tip is fully embedded in the non-

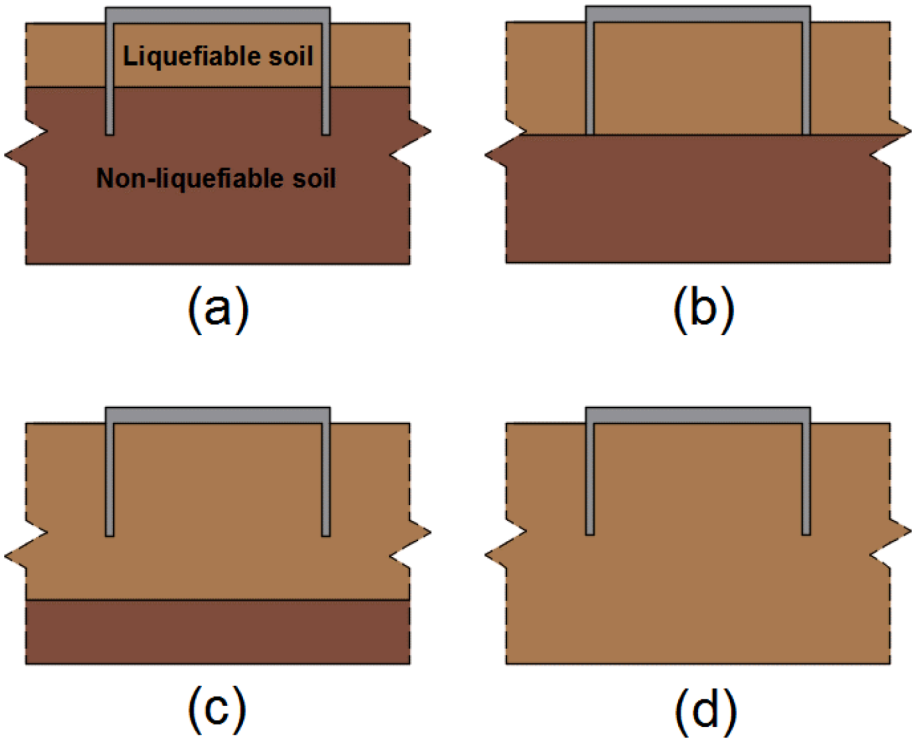

Fig. 15. Idealized soil layering conditions with different depths of liquefiable layer: a) 3 m b) 7 m c) 11 m d) 15 m.

liquefiable soil (Fig. 15(a)), the second condition with $t_{s,l}$ = 7 m, the skirt's tip is located right at the interface of the liquefiable and the non-liquefiable soil (Fig. 15(b)). On the other hand, the third and fourth conditions consisted of liquefiable soil 11 m and 15 m deep in the former and latter models where the caisson foundation is entirely situated in the liquefiable soil and in the loose sand extending all the way down to the bottom boundary, respectively (Fig. 15 (c) and (d)). The effect of specific density of overlying soil on the foundation settlement was investigated alongside.

An approximate procedure was developed by Davisson and Robinson (1965) to evaluate the buckling problem in partially embedded piles. In this procedure, the pile was assumed as a free-standing pile with equivalent length (L_{eq}), and a fixed base. This approach was later verified in centrifuge models reported by Bhattacharya (2003).

In this method, depth of fixity for piles were taken as 1.8 T, where T, the relative stiffness of soil and pile, is expressed as:

$$T = \sqrt[5]{EI/\eta_h} \tag{26}$$

where E and I are pile's Young modulus and moment of inertia, respectively, and η_h is soil's modulus of subgrade reaction. According to the formulation above, an attempt had been made to calculate the unsupported length so called depth of fixity for the considered cases ranging between 5.2 m and 6.6 m.

But nevertheless, results in Fig. 16 indicate that when $t_{s,l}$ is shorter than the skirt length, settlement and tilting become negligible, primarily due to the partial contribution of skirt friction and end bearing resistance of skirt tip in non-liquefiable deposit. Rather instead, the results reveal the existence of a clear-cut point nearly 3.5 m below the skirt tip in liquefiable layer regardless of varying soil density, where within which foundation exhibits insignificant punching settlement when the caisson is fully founded on liquefiable soil.

Once liquefaction happens, the soil surrounding the pile loses its effective confining stress and may not offer sufficient bearing resistance. The pile may then act as an unsupported column prone to axial instability (Bhattacharya, 2003). In this plane-strain simulation, skirt's settlement pattern resembles pile's settlement behavior in liquefiable soils due to large aspect ratio. Unlike the Davisson and Robinson (1965) formulation, skirts most likely prevent large foundation settlement due to end bearing resistance of skirts' tips embedded sufficiently in the non-liquefiable layer below the liquefiable layer as well as the inner skirt friction which remained almost unchanged during wave action (i.e., due to dilation-induced restiffening development, see Figs. 12-14). This limited punching may be attributed to sufficient post-liquefaction strength and to a lesser extent to the dilative sand response which caused to prevent complete bearing failure and arrest of shear strains development.

Of note, although the direct proportionality between the settlements and the initial thickness of the liquefiable layer ($\frac{t_{s,l}}{h}$ = 0.2, 0.466) were consistent with the other experimental work and case histories were the liquefiable layer was relatively thin (Liu and Dobry, 1997; Hausler, 2002), beyond which, settlements are not directly linked to the thickness of liquefiable soil and maybe a misconception. It can be inferred that, while increasing the thickness of the liquefiable layer likely intensify volumetric-induced settlement, a significant settlement results from deep seated slumping and bearing capacity failure (deviatoric mechanisms), more so than volumetric strains development. This is likely the reason for the disparity between the results and has previously evaluated in other liquefaction-induced ground failures. For example, in an attempt to relate the observed severity of levees damage mechanisms to the thickness of liquefied layer, liquefiable layer thickness was shown to be insufficient in assessing the damage severity and levee response on softened ground (Green et al., 2011).

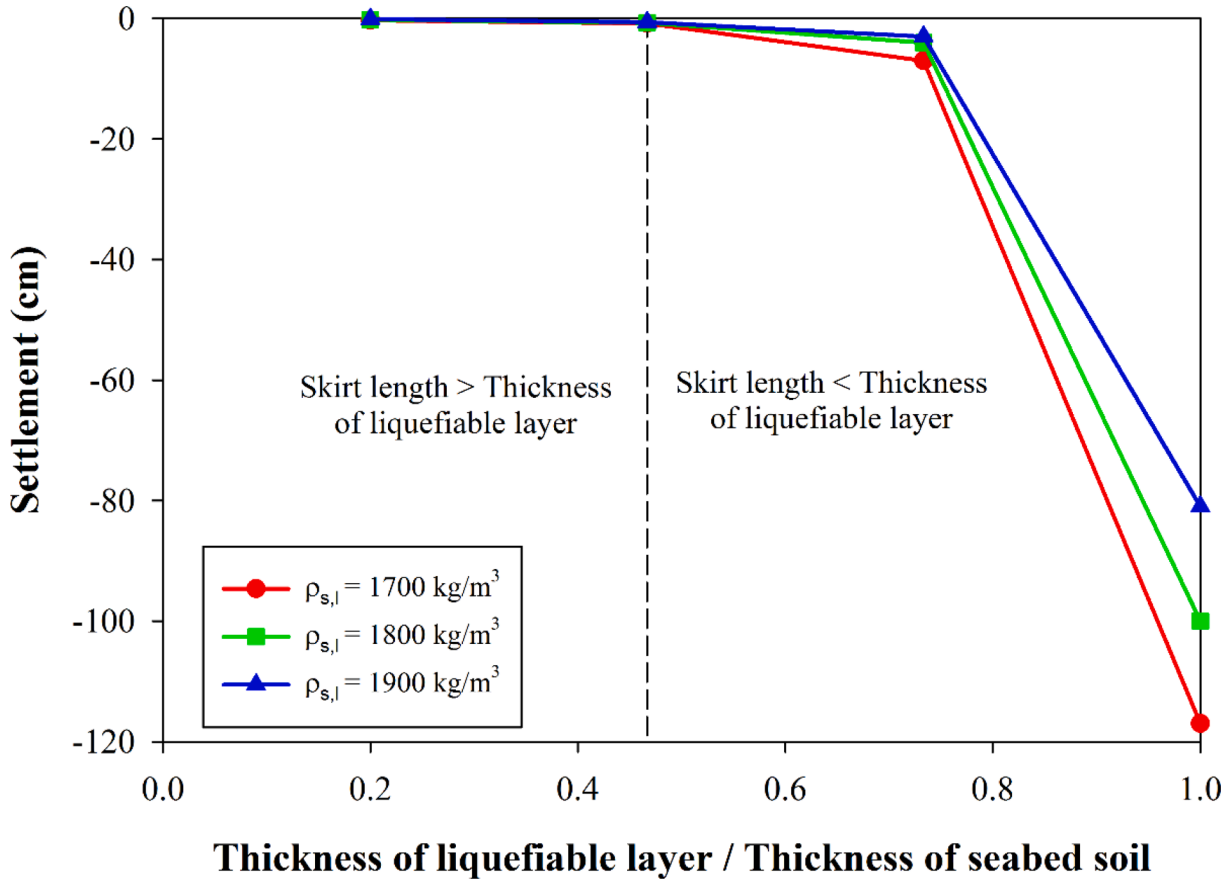

Fig. 16. Foundation settlement versus normalized thickness of liquefiable layer.

On the other hand, when $t_{s,l}$ is longer than the skirt length, excessive settlements might happen during the wave-induced liquefaction in particular in fully liquefiable sandy seabed due to the softening resulted from pore pressure generation. In addition, as $t_{s,l}$ increases, effect of the different densities of the liquefiable layer becomes more evident due to sudden increase of shear strains.

(b) Influence of OWT weight.

Of special interest here in this section, was to present significant trends for liquefaction-induced caisson settlement against site parameters, $t_{s,l} = 3$ and 11 m and contact pressure $q = 25$–300 kPa induced by varying OWT superstructure mass. It is obvious from Fig. 17 that the liquefaction-induced settlement versus site parameters have been greatly influenced by wave cycle number through examination of the effective stress analyses. There has been found a significant interacting impact from wave action duration and state parameters and thus intensifying the liquefaction manifestation and punching the foundation into softened ground. The shallow foundation contact pressure was identified here as key state parameter through examination of the numerical results. Fig. 17 shows liquefaction-induced settlement increases as the contact pressure of the OWT systems with tip located on non-liquefiable soil increases towards a distinct value ($q = 100$ kPa), while further increase of OWT weight has adverse effect. The higher values of excess pore pressure induced by a threshold contact pressure (i.e. q >∼ 100 kPa) mayn't be sufficiently enough, most likely due to embedded skirt portion into the underlying non-liquefiable soil in the excess of 0.55 to compensate initial vertical effective stress, σ'_{v0}. Contrary to Fig. 17, Fig. 18 suggest that heavier turbine may intensify larger amount of excess pore pressure generations and settlement mechanisms of a caisson.

(c) Influence of the caisson geometry

Examination of the trends in the results obtained from FE simulations provided an insight into the effects of key geometrical parameters on the settlement resulting from wave-induced liquefaction.

The thickness of the liquefiable soil was considered 11 m with the diameters 10 m and 14 m inscribed by skirt length ranged 4–13 m, keeping all else unchanged.

It is noteworthy to mention that by comparing settlement results between Fig. 19(a) and Fig. 19(b), it is revealed that the settlement of smaller diameter caissons is likely less influenced by seabed soil density variation. A decrease in diameter (from 14 m to 10 m) may amplify the ability of excess pore water pressures to dissipate rapidly from within

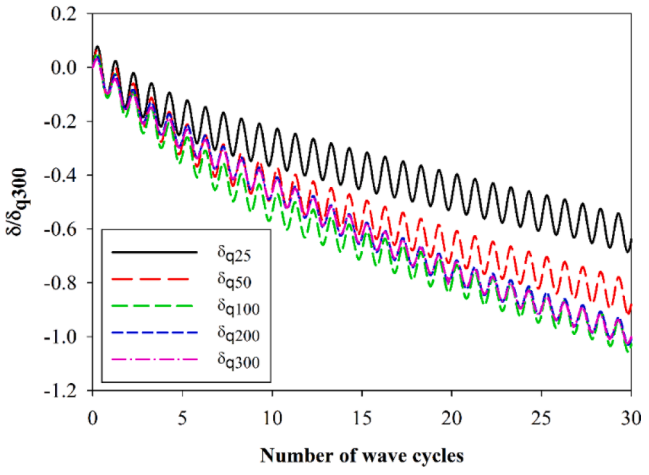

Fig. 17. Foundation's normalized settlement during 30 cycles of wave loading for liquefiable soil's depth of 3 m.

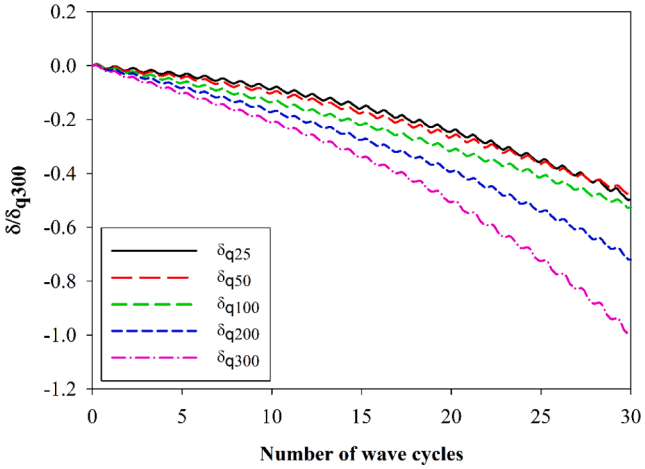

Fig. 18. Foundation's normalized settlement during 30 cycles of wave loading for liquefiable soil's depth of 11 m.

the caissons by reducing the drainage path (i.e., amplify the contribution of consolidation-induced settlements). Contrarily, wider caissons may result in a remarkable reduction in settlement in comply with the more sustained net excess pore pressures, wherein the development of EPP is strongly influenced by the sand relative density, its stiffness and resistance to softening/bearing failure of the OWT and its tendency to dilate. Fig. 19 further demonstrates that for the same OWT, the shallower foundation experiences greater settlement.

Because of the smaller contact area, smaller diameter generates higher contact pressure compared to wider foundation in Fig. 19; therefore, facilitates foundation settlement during the cyclic loading (e.g., an increase from 57 cm to 89 cm for $\rho_{s,l} = 1700\,\mathrm{kg/m^3}$, and from 24 cm to 72 cm for $\rho_{s,l} = 1900\,\mathrm{kg/m^3}$). Besides, the higher contact pressure, amplified the OWT settlement caused primarily by bearing capacity failure strains (ε_{q-BC}) but the settlement was perhaps less influenced by the localized volumetric strains due to drainage near the caisson tip.

5.4. *Wave-induced bearing capacity degradation.*

Foundations under cyclic loading are known to experience reduction of bearing capacity resulted from pore pressure accumulation (Karamitros et al., 2013) and changes in soil-structure normal contact stress (Poulos, 1989; Achmus et al., 2020; Zhao et al., 2020). To evaluate the effect of wave-induced liquefaction on bearing capacity of suction caisson, bearing capacity ratio (*BCR*) is defined as:

$$BCR = \frac{DBC}{BC} \tag{27}$$

where, *DBC* and *BC* are the degraded bearing capacity in liquefied soil and bearing capacity in non-liquefied soil, respectively. It should be pointed out that higher *BCR* indicates higher resistance of foundation to severe settlement driven by static stresses. Bearing capacity ratio can be estimated with respect to results of numerical simulations based on the steps illustrated in Fig. 20:

- *Step 1*: Gravity load was applied to stabilize the soil condition for complementary analyses and stablishing the benchmark settlement ($\delta_{\mathrm{gravity}}$).
- *Step 2*: Static load was applied on the foundation until reaching the limiting value of settlement (approximately $0.1D_b$) to calculate the bearing capacity (*BC*).
- *Step 3:* In a separate simulation, after the completion of gravity analysis, 30 cycles of wave loading was exerted on the seabed surface which led to pore pressure generation and occurrence of liquefaction in certain depths and finally resulted in cyclic settlement (δ_{cyc}).

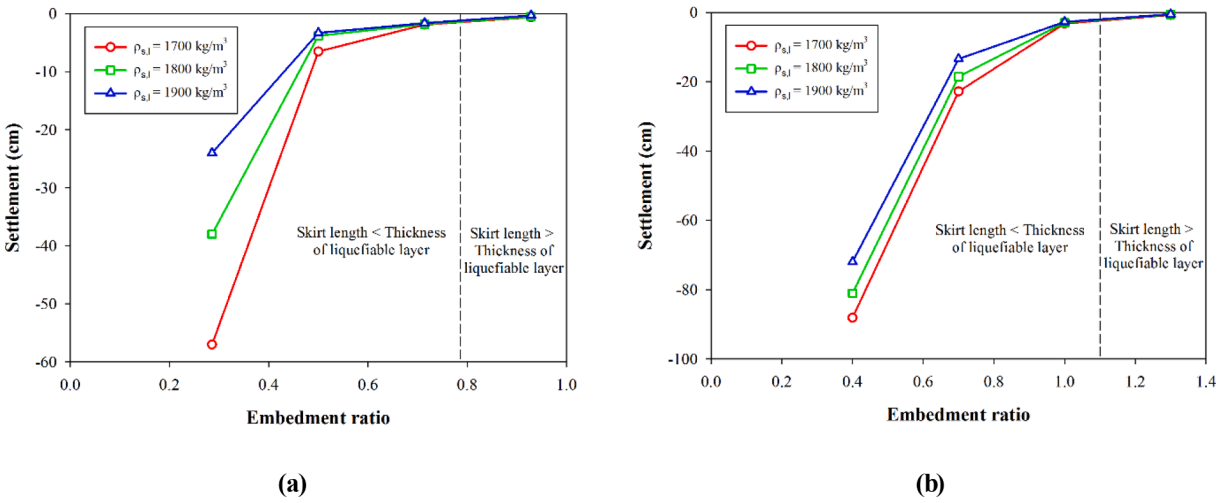

Fig. 19. (a) Foundation settlement versus normalized skirt length for (a) caisson diameter of 14 m (b) caisson diameter of 10 m.

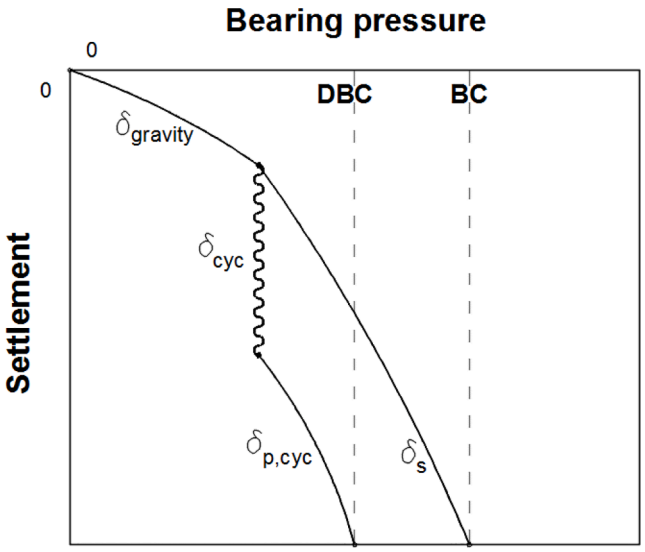

Fig. 20. Scheme of bearing pressure-settlement curves.

Following this, by applying the static load gradually, degraded bearing capacity (*DBC*) was obtained, when the desirable post-cyclic settlement ($\delta_{p,cyc}$) was achieved. In this specific study, analyses were performed for suction caisson foundations with various skirt lengths, (L_s = 4, 7 and 10 m; i.e. embedment ratio = 0.28, 0.5 and 0.71) founded in a fully-liquefiable and a layered seabed. Moreover, a shallow foundation (embedment ratio = 0) was taken into account in analyses as well, allowing to isolate the individual contribution of embedment ratio to the bearing capacity of offshore foundations. The properties of soil and foundation remained the same as those in section 5.1, except for the specific density of foundation which was reduced considerably to minimize the effect of gravity analyses on initial settlement.

Fig. 21 shows bearing pressure-settlement curves for a typical soil ($\rho_{s,l}$ = 1800 kg/m^3). Numerical results reveal that as the embedment ratio increases, bearing capacity of foundation increases correspondingly. This is due to the frictional resistance of both inner and outer surfaces of skirts (Barari et al., 2017b). Also, it can be inferred from the results that presence of non-liquefiable soil at the bottom of the seabed (Fig. 15 (c)), increased both bearing capacity and degraded bearing capacity of suction caisson, specifically for higher embedment ratios.

By initiation of settlement, the applied vertical pressure was carried by tip and skin resistance; however, the soil mass confined within the caisson appeared to act as a uniform rigid body gradually causing coring phenomena, which explains the initial curved pattern and subsequent linear, uniform pattern of caisson foundation settlement (Vincent et al., 2020). Moreover, as discussed in section 5.1, the soil within the caisson did not reach the liquefaction stage due to the confining impact of skirts and the less intense waves cyclic forces; consequently, the stiff, linear settlement pattern of foundation might stem from the higher shear resistance of non-liquefied soil within the caisson.

There are various approaches to estimate the bearing capacity of foundations, however, as there is no distinctive failure pattern in load-settlement curves, other approaches are now acknowledged to estimate the bearing capacity for example 0.1B method, log–log approach, and tangent intersection method (TIM) (Cerato, 2005; Kolay et al., 2013). In this study, 0.1B method was chosen to examine bearing capacity and degraded bearing capacity of foundation. However, in spite of possible underestimation of bearing capacity in 0.1B method, it was convenient to obtain *BCR* values.

In Fig. 22, *BCR* versus embedment ratio is presented for various specific densities of liquefiable soil. Results show that increase in embedment ratio contributes to increase in *BCR*. It is revealed that presence of skirts acted as remedial measure to increase the ultimate caisson *BCR* by about 44% for the lower specific density ($\rho_{s,l}$ = 1700 kg/m^3) and embedment ratio of 0.86 (compared with surface footing namely benchmark model). The same consistent scenario was reported in Adalier et al. (1998) by using an experimentally retrofit procedure using sheet pile enclosure. Local pore-pressure and underlying liquefied soil migration from benchmark foundation beneath that may occur as the hydraulic gradients generated, are identified as main cause of formation of significant localized volumetric strains/deviatoric strains in the soil in the vicinity of foundation. Therefore, the inclusion of skirts resulted in partial containment of the foundation soil. The skirts eliminated the kinematic deformation mechanisms and resultant settlement.

However, it can be seen that by increasing the liquefiable soil density, *BCR* became less sensitive to the variation of embedment ratios. For instance, for $\rho_{s,l}$ = 1700 kg/m^3, by the increase in embedment ratio, BCR increased from 0.55 to 0.93. However, for $\rho_{s,l}$ = 1900 kg/m^3, *BCR* increased from 0.7 to 0.9. The enhanced performance in liquefied soils (i.e., particularly when embedment ratios are highest) gave the highest bearing capacity ratio which is consistent with experimental observations (Ahidashti et al., 2019).

Moreover, comparison between Fig. 22 (a) and (b) demonstrates that presence of non-liquefiable layer at the bottom of the seabed (Fig. 15 (c)), adversely reduced the *BCR* of foundations with relatively low

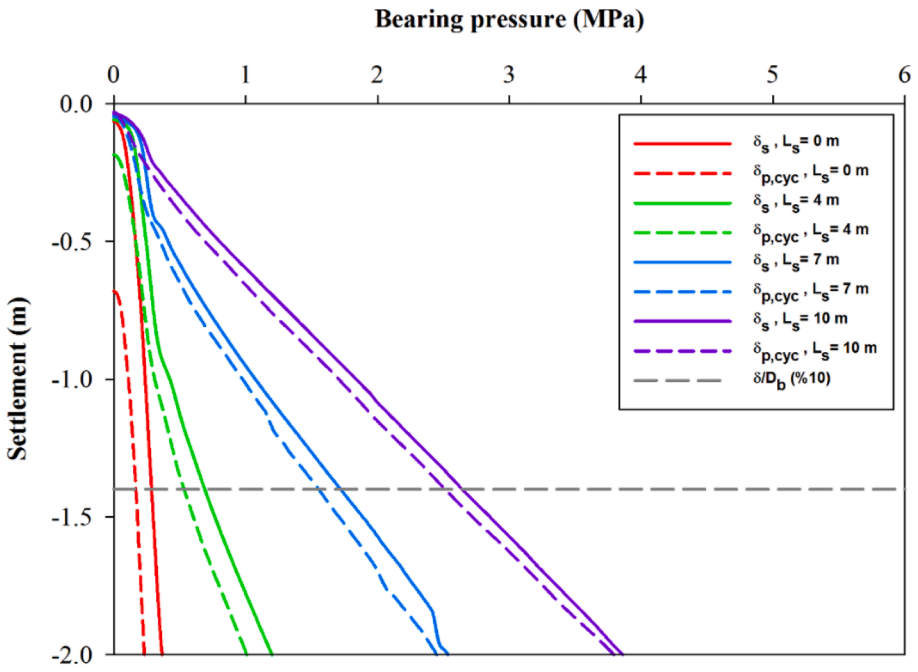

(a)

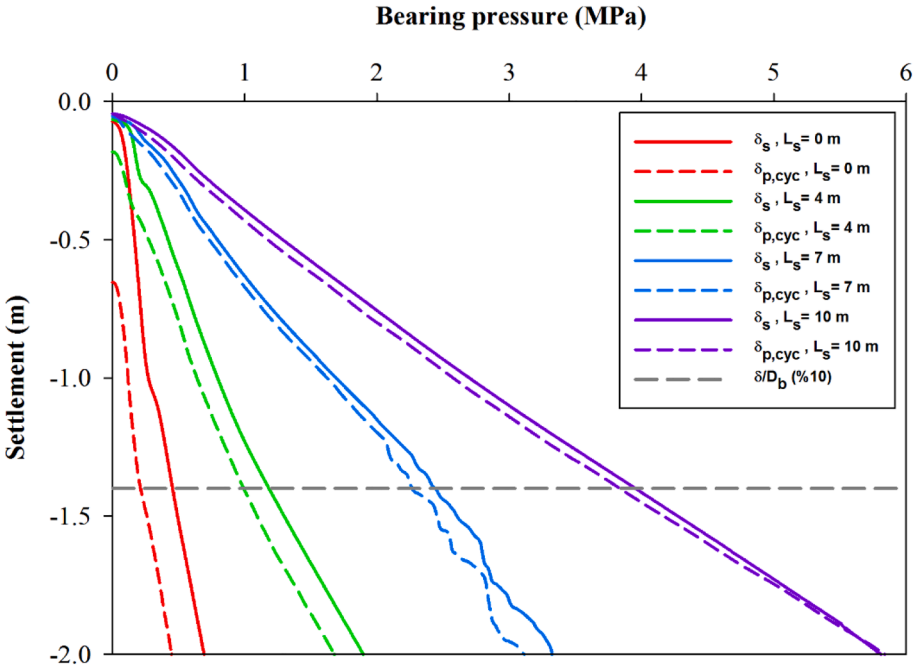

(b)

Fig. 21. Numerical results of bearing pressure-settlement curves ($\rho_{s,l} = 1800\,kg/m^3$) for a) fully-liquefiable seabed, b) layered seabed.

values of embedment ratio. Also, it is revealed that in the presence of non-liquefied layer at the bottom of seabed (Fig. 22 (b)), for higher embedment ratios (e.g., 0.5 and 0.71), *BCR* remained insensitive to variation of specific density of the liquefiable layer.

5.5. Effect of loading characteristics on bearing capacity ratio

In this section, the interplay between wave loading characteristics (*H*, *L*,*T* and *d*) and *BCR* is evaluated by the means of EPWPR (r_u) at critical region beneath the foundation. The model condition was as same as section 5.1. As shown in Fig. 23, for a suction caisson foundation with

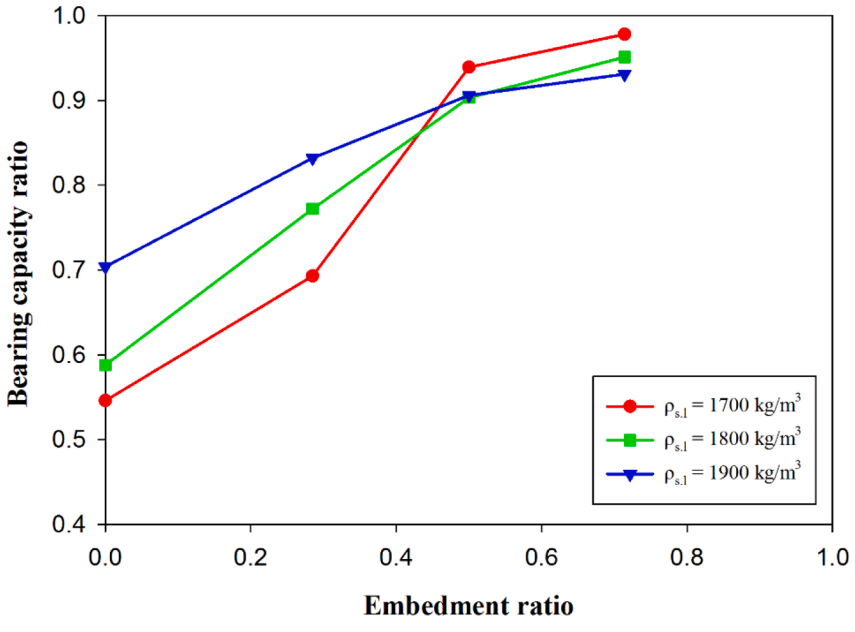

(a)

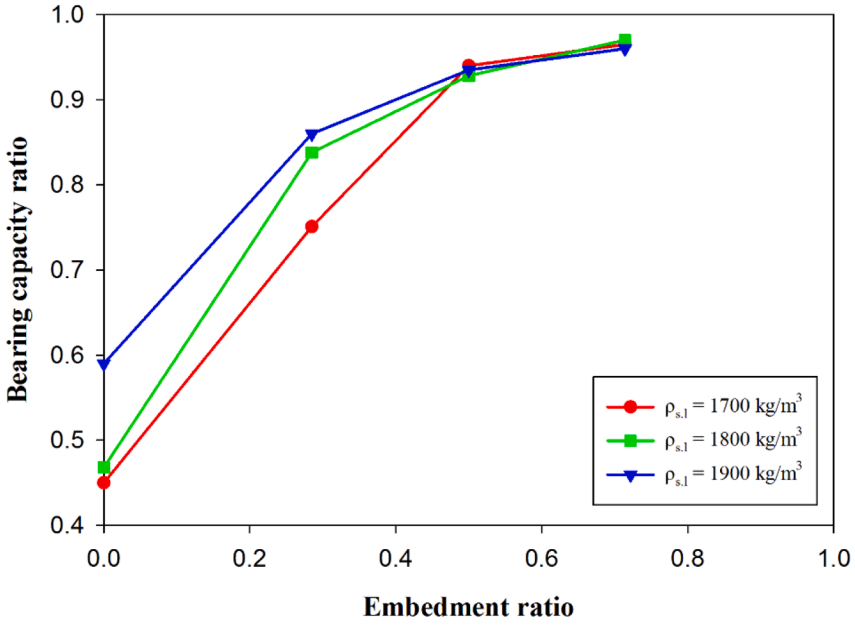

(b)

Fig. 22. *BCR* versus normalized skirt length for different specific densities of a) fully-liquefiable soil, b) layered soil.

embedment ratio of 0.5, *BCR*s greater than 0.9 is expected due to the important role the embedment ratio plays in the increase of the *BCR*. A weighted average of EPWPR around the tip (U_{tip}) and underneath the centerline of foundation (U_{bucket}) was adopted for the numerical solution as $r_u = (U_{tip} + U_{bucket})/2$. Fig. 23 (a) demonstrates that as the r_u increased, the *BCR* declined, highlighting the confrontational effect of EPWP accumulation on degrading the bearing capacity of foundations. In addition, it can be observed that as H and L increased, r_u rose, however, the increase in T and d adversely affected r_u. Moreover, Fig. 23 (b) shows that in spite of the high scatteredness of data for higher values of EPWPR ($r_u \cong 1$), a quadratic fitted curve can reasonably predict the influence of loading characteristics on the EPWPR variation and the following changes in bearing capacity ratio of foundation. Based on the r_u generated by different wave characteristics, the closed-form solution presented below can predict the *BCR* of offshore foundation under the action of waves.

$$BCR = 1 - 0.145r_u + 0.07r_u^2 \tag{28}$$

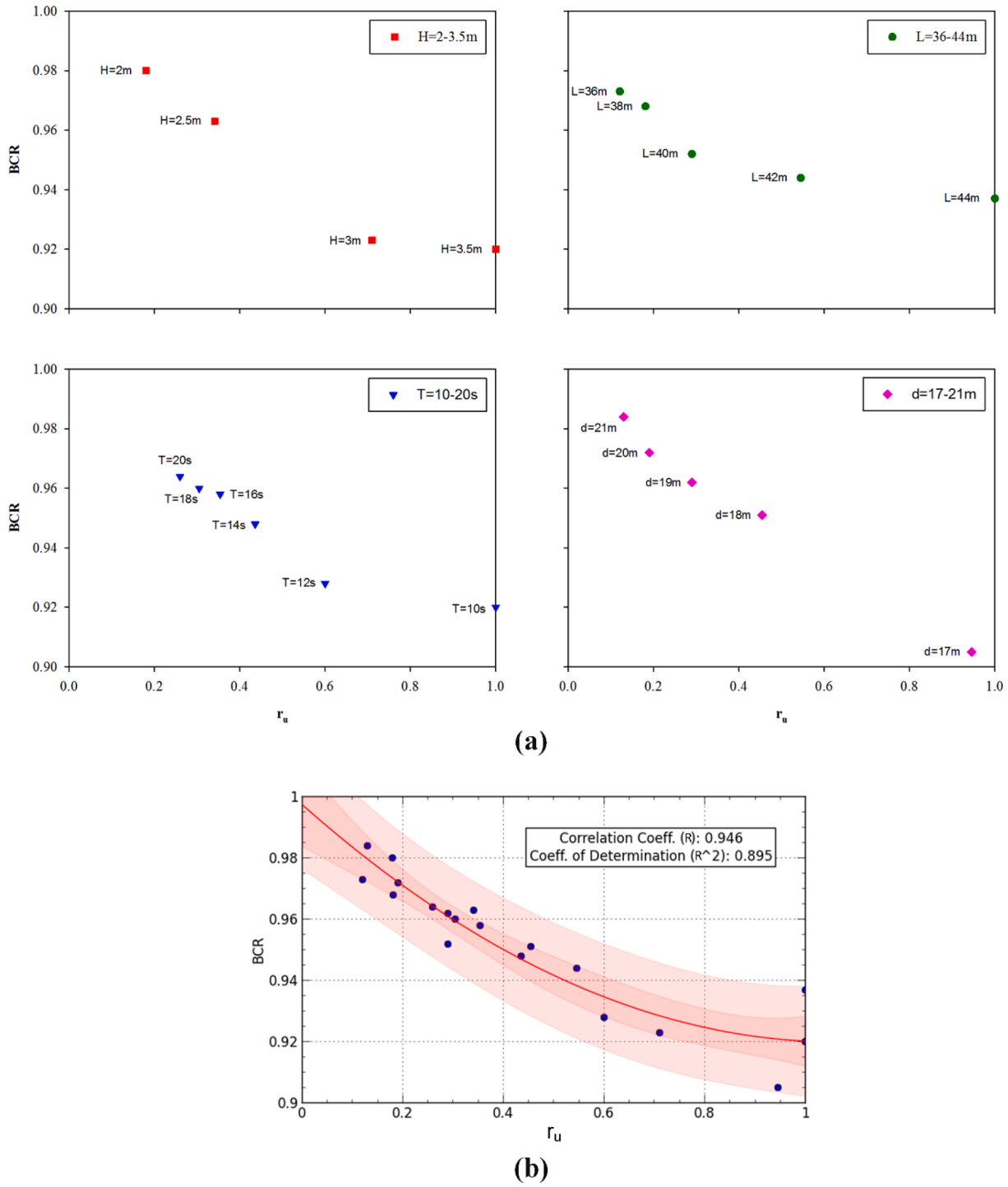

Fig. 23. (a) Effect of loading characteristics on EPWPR and the subsequent bearing capacity degradation, (b) the fitted curve predicting influence of loading characteristics on bearing capacity degradation.

5.6. Results of nonlinear dynamic analysis to predict wave-induced caisson settlement.

In this section, first, FE nonlinear dynamic analyses are performed considering different seabed characteristics, structural parameters and wave heights in order to obtain the settlement of suction caisson foundation under a range of different model configurations; then, ANN-based approaches are put to practice to introduce an analytical framework predicting wave-induced caisson settlement.

5.6.1. Settlement results of analytical dynamic simulations

There are three key mechanisms of wave-induced caisson settlement (S_w) including: ejecta-induced, volumetric-induced and shear-induced settlements, amongst which shear-induced deformation is the predominant one and can be estimated with the aid of effective stress nonlinear dynamic analyses. Sensitivity analyses are performed to evaluate the effect of different wave characteristics, structural configuration and seabed condition on the amount of wave-induced caisson settlement. All parameters affecting the settlement pattern are tabulated in Table 4 along with the baseline model. According to 25 different model setups,

Table 4
Model parameters for nonlinear FE analyses.

Parameter	Values	Baseline case
Relative density of liquefiable layer, D_r (%)	40, 60, 80	40
Thickness of liquefiable layer, $t_{s,l}$ (m)	1, 3, 7, 11, 15	11
Caisson diameter, D_c (m)	10, 14	14
Skirt length, L_s (m)	1, 4, 7, 10, 13	7
Embedment ratio, E_r	0.07, 0.28, 0.5, 0.71, 0.93	0.5
Contact pressure, Q (kPa)	200, 300, 400, 488, 600, 700	488
Tower height, H_t (m)	120, 160, 200, 230	160

250 simulations are performed and analyzed. Using multiple cores of HPC facilities for parallel analyses in order to reduce the computing time, each analysis took 12 to 33 h to be done completely based on the model configurations. Wave heights (H) varied from 1 to 10 m is chosen as the parameter determining dynamic wave pressure (loading intensity). The relative density of the liquefiable layer (D_r) is ranged from 40% to 80% with the thickness ($t_{s,l}$) from 1 to 15 m. Based on the caisson diameters (D_c) selected as 10 and 14 m and also the skirt lengths (L_s) ranged from 1 to 13 m, the embedment ratio (E_r) is varied from 0.07 to 0.93. The OWT contact pressure (Q) varied from 200 to 700 kPa for approximate prediction of 3.6 to 15 GW OWT output capacities. OWT tower heights (H_t) of 120 to 230 m are considered in this study. Key trends and important parameters affecting the shear-induced settlement caused by the waves are identified by performing the cyclic WSFI effective stress analyses as a part of this study. The relative density (D_r) and the thickness of the liquefiable seabed layer ($t_{s,l}$) are determined as key seabed parameters through assessment of the numerical simulations. Results of a subset of analyses on representative trends for wave-induced caisson settlement is shown in Fig. 24. A nearly linear pattern of settlement for different relative densities can be observed for lower loading intensities (i.e., H = 1 to 5 m); however, the wave-induced settlement increases significantly for higher loading intensities (i.e., H = 6 m and above) in loose sand (i.e., D_r = 40%) (Fig. 24 (a)). Fig. 24 (b) reveals that except for the lowest loading intensity (i.e., H = 1 m), a sudden increase in settlement occurs as $t_{s,l}$ increases. For mild loading intensities (i.e., H = 2 to 5 m), the sudden settlement occurs when $t_{s,l}$ exceeds 11 m and for harsh loading intensities (i.e., H = 6 to 10 m), the sudden settlement take place when $t_{s,l}$ exceeds 7 m.

Taking into account the structural parameters of the caisson, the embedment ratio (E_r) and the contact pressure (Q) are identified as key parameters influencing the wave-induced settlement. This is shown in Fig. 24 (c) that as the loading intensity increases, the settlement pattern tends to initiate its increasing rate at higher embedment ratios. For example, the increasing rate initiates for E_r = 0.28 at H = 1, 2 and 3 m, while for E_r = 0.93 it begins at H = 6 m. Also, it is noteworthy to mention that the curves resemble a hyperbolic tangent shape. Regarding to influence of foundation contact pressure (Q) on wave-induced settlement, although a moderately steep increase of settlement is observed for Q = 400 kPa, the foundation settles in a nearly linear manner, which can be considered as a key parameter for the development of wave-induced settlement relationship (Fig. 24 (d)). In spite of the fact that OWT tower height (H_t) does not play a major role in the current framework and its effect can be fairly captured through the contact pressure analyses.

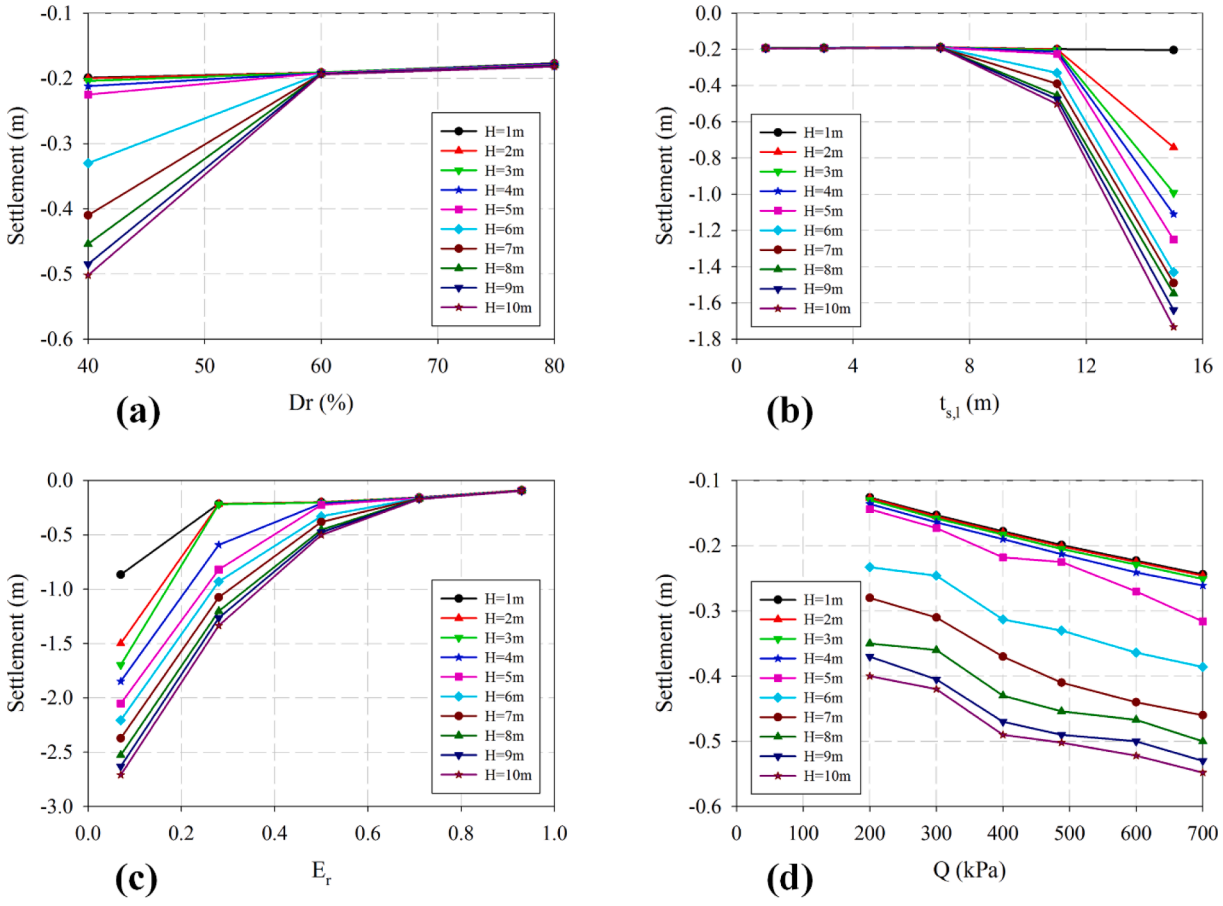

Fig. 24. Effect of key model parameters on wave-induced caisson settlement for different loading intensities (H = 1–10 m): (a) effect of relative density (D_r), (b) effect of thickness of liquefiable layer ($t_{s,l}$), (c) effect of embedment ratio (E_r) and (d) effect of contact pressure (Q).

5.6.2. A neural network-aided function to predict wave-induced caisson settlement

Ivakhenko (1971) has initially proposed a neural network-based method known as Group Method of Data Handling (GMDH) using the repetition of a series of multilayered perceptron type network structures. GMDH is known for the capability of solving extremely complex nonlinear problems. Concerning this method, a prediction numerical model can be developed as a set of neurons in which several pairs of them in each layer can be implemented through a second-order polynomial function and, therefore, generate new neurons in the next layer based on the artificial neural network (ANN).

In other words, GMDH method employs several layers to find the best relationship between independent variables and outputs while the generation of each layer containing low-impact variables are ignored and more effective variables can be used to construct next layer. According to the Farlow (2020) and Nariman-Zadeh et al. (2002), GMDH algorithm attempts to find the relationship between correlated inputs X_i and demanded target outputs Y given as follows:

$$Y(x_1, x_2, x_3, \cdots, x_n) = C_0 + \sum_{i=1}^{m} a_i \Lambda_i \tag{29}$$

where C_0 represents contact coefficient and a_i is the ith weighting coefficients. In addition, it is expected that function Z can presents accurate approximation of function dealing with reducing amount of occurred error for input vector $X = (x_1, x_2, x_3, \cdots, x_n)$. Minimizing least square error (LSE), a set of quadratic models are implemented to achieve the optimal model which is trained according to the considered indices (Nazarimofrad et al., 2019). One is needed to make ANN method more accurate that the differences between the real output and the predicted one should be minimized as follows:

$$\sum_{i=1}^{m} [\widehat{f}(x_{i1}, x_{i2}, x_{i3}, \cdots, x_i) - y_i]^2 \rightarrow min \tag{30}$$

According to the Ivakhnenko (1971), a few sentences of the Volterra functional series known as Kolmogorov-Gabor polynomial can be employed to make the proposed approach more practical given as follows:

$$\widehat{S}_{i,j} = G(x_i, x_j) = q_{i,j} = a_0 + a_1 x_i + a_2 x_j + a_3 {x_i}^2 + a_4 {x_j}^2 + a_5 x_i x_j \tag{31}$$

where $\widehat{S}_{i,j}$ denotes the polynomial in the layer which is developed utilizing the combination of two input variables with indexes i and j, respectively. In addition, coefficients $(a_0, a_1, \cdots, a_5)$ are weighting coefficients that used for implementing the relationship between all variables.

Concerning next layer, the ANN algorithm uses following least-squares error (LSE) to select neurons which are fitted for next generation:

$$\text{LSE} = \frac{\sum_{i=1}^{m} (S_i - G_i)^2}{m} \rightarrow min \tag{32}$$

Once a specified level of error is obtained, this iterative algorithm stops, and the final optimal function is proposed. The overall scheme of the considered GMDH network is represented graphically in Fig. 25.

In the current study, after learning and training of the proposed GMDH network, the final optimal function estimating wave-induced caisson settlement is proposed. Table A1 in Appendix 1 presents the characteristics of input data for selected parameters. In addition, a summary of statistical parameter of inputs is presented in Table 5. As depicted in Fig. 26, the best structure of GMDH model, which has robust performance to predict wave-induced caisson settlement is developed by many trials and errors. It is worth noting that each neuron in all layers is implemented by a second-order polynomial.

Considering the first layer of proposed ANN model, there are four quadratic polynomials (q_1, q_2, q_3, q_4) in which each of them is proposed based on the combination of two input variables using Eq. (31).

$$q_1 = -0.1522 - 0.0483 D_r - 0.0717 E_r - 1.9004 \times 10^{-4} {D_r}^2 - 3.8269 {E_r}^2 + 0.1512 D_r E_r \tag{33}$$

Table 5
Statistical parameters of inputs data.

Parameter	$D_r(\%)$	$t_{s.l}(m)$	$E_r(-)$	$Q(kPa)$	$H(m)$
Maximum	80.00	15.00	0.93	700.00	10.00
Minimum	40.00	1.00	0.07	200.00	1.00
Median	40.00	11.00	0.50	488.00	5.50
Average	43.16	10.05	0.49	475.37	5.50

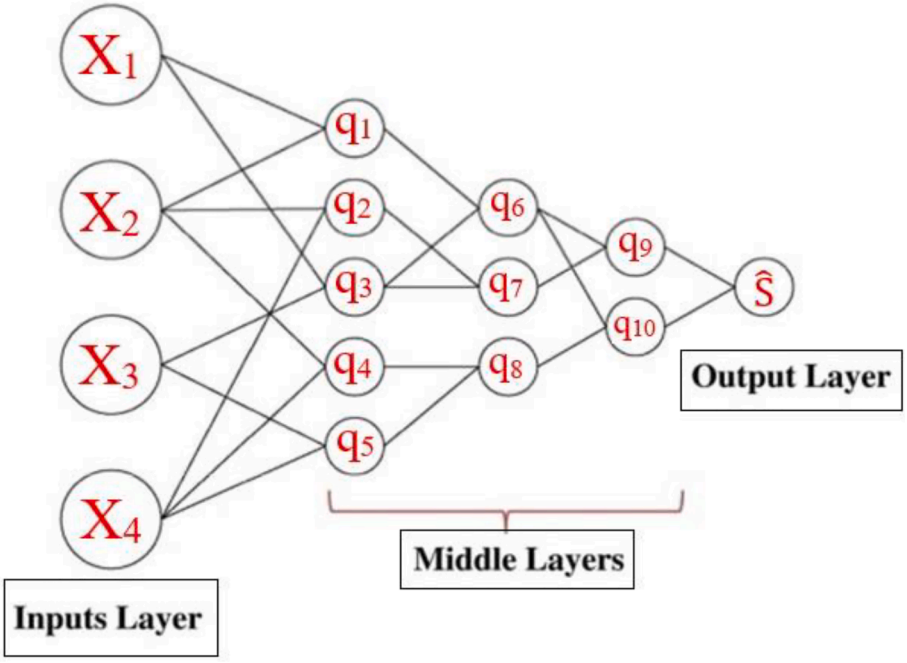

Fig. 25. Illustration of GMDH approach.

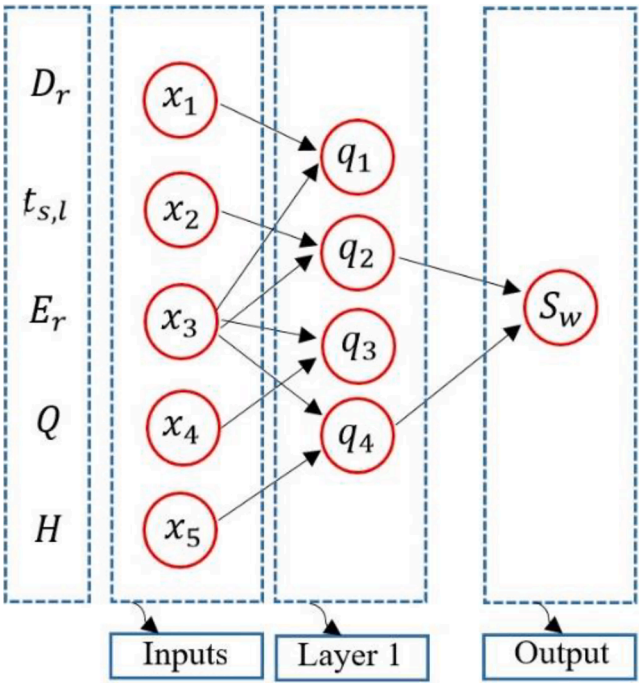

Fig. 26. Final scheme of the proposed GMDH model.

$$q_2 = 0.4003 - 0.0915t_{s,l} + 0.2540E_r - 0.0150{t_{s,l}}^2 - 4.1192{E_r}^2 + 0.5468t_{s,l}E_r \tag{34}$$

$$q_3 = 0.7832 + 0.3916E_r - 0.0070Q - 3.8721{E_r}^2 + 1.0916 \times 10^{-6}Q^2 + 0.0115E_rQ \tag{35}$$

$$q_4 = -1.4123 + 4.5882E_r - 0.1637H - 3.8962{E_r}^2 - 0.0010H^2 + 0.2531E_rH \tag{36}$$

Concerning the last layer, final generalized equation for estimating wave-induced settlement of OWTs is developed based on the above-mentioned equations:

$$S_w = 0.0055 + 0.7044q_2 + 0.2051q_4 - 0.2023{q_2}^2 - 0.5432{q_4}^2 + 0.6998q_2q_4 \tag{37}$$

Moreover, to evaluate the accuracy of the developed equation, four parameters including coefficient of determination (R^2), mean-squares error (MSE), root mean-squares error (RMSE) and mean absolute deviation (MAD) are used given as follows (Farahani and Akhaveissy, 2022):

$$R^2 = 1 - \frac{\sum_{i=0}^{M}\left(Y_{i(model)} - Y_{i(actual)}\right)^2}{\sum_{i=0}^{M}\left(Y_{i(model)} - \frac{1}{M}\sum_{i=1}^{M}Y_{i(model)}\right)^2} \tag{38}$$

$$MSE = \frac{\sum_{i=0}^{M}\left(Y_{i(model)} - Y_{i(actual)}\right)^2}{M} \tag{39}$$

$$RMSE = \sqrt{\frac{\sum_{i=0}^{M}\left(Y_{i(model)} - Y_{i(actual)}\right)^2}{M}} \tag{40}$$

$$MAD = \frac{\sum_{i=0}^{M}\left|Y_{i(model)} - Y_{i(actual)}\right|}{M} \tag{41}$$

Fig. 27 shows a comparison of the predicted results from the developed Eq. (37) (i.e. outputs in ANN neural model) with those obtained by cyclic analysis (i.e. targets in ANN neural model). It is evident from Fig. 27 that the trained GMDH neural model can well estimate the observed results from cyclic analysis. In addition, as can be seen in Fig. 27 (c), the proposed GMDH network follows the behavior of all data as well.

Furthermore, the difference between each sample and its original value is determined by obtained error as shown in Fig. 28. It is also apparent from Fig. 28 that the values for MSE and RMSE parameters (Eqs. (39) and (40)) for all data were obtained as 0.034309 and 0.18523, respectively. The histogram of the mean error and the standard deviation error of each set of data can be found in Fig. 28 as well.

Fig. 29 illustrates the comparison of observed settlement with those calculated with Eq. (37). To evaluate the accuracy of the proposed equation, the horizontal axis outlines the settlement obtained by FE analysis, and the vertical axis represents the settlement estimated by Eq. (37). The error estimation line defined as the ratio of results obtained from the proposed Eq. (37) to the results observed in FE analysis, when both of the results are equal has also been illustrated in Fig. 29. As shown in Fig. 29, compared to the results obtained from FE simulations, overall, the proposed equation can reasonably predict the wave-induced caisson settlement. In addition, the coefficients of determination (R^2) for the developed equation were also obtained 0.93108, 0.93469 and 0.93151 for Train data, Test data and All data, respectively. It is worth noting that the current analyses are performed for a limited subset of seabed and caisson configuration which do not cover highly variable soil and structure parameters; Also, in comparison to other studies conducted for settlement prediction of shallow foundations under seismic loading (Palacios et al., 2022), there are more soil-foundation interaction complexities when it comes to the case of wave-induced settlement of offshore skirted foundations; therefore, caution is warranted when using the proposed equation.

6. Conclusions

In this study, geotechnical aspects of residual wave-induced liquefaction around suction caisson for offshore wind turbines founded on layered sandy seabed was evaluated, while special attention was paid to wave-seabed-foundation interaction (WSFI). Biot's consolidation theory, linear wave theory and the CycLiqCPSP elasto-plastic constitutive soil model were employed to capture the soil response in code-based framework implemented in OpenSees finite element software. Soil model parameters were calibrated against CSS tests and the numerical model was validated by a well-documented centrifuge experimental model. A reasonably efficient analytical function based on an ML-inspired group method of data handling was developed for estimating wave-induced caisson settlement. On the basis of the numerical results, the following conclusions can be drawn:

The numerical results indicate that pore pressure buildup within the caisson was slower than regions around the caisson because of the confining impact of skirts around the soil. In addition, longer drainage path and the dilative behavior of sand within the caisson, made the sand response even more complicated. Moreover, as the density of sand increased, more cycles of wave loading were required for sandy seabed to be liquefied. Stress paths of monitoring points demonstrated that the transformation of sandy seabed from pre-liquefaction to post-liquefaction states due to the decrease in effective stresses was greatly affected by the state parameters (i.e., confining pressure, static shear stress and specific density of the liquefiable layer).

A comprehensive study was conducted to assess the influence of seabed characteristics (specific density of liquefiable layer and seabed layering condition), geometrical properties of suction caisson (skirt length and caisson diameter) and OWT weight on foundation settlement. Overall, an increase in thickness of liquefiable layer increased the foundation settlement. However, the strength of underlying soil into which tip penetrated was identified as the key parameter controlling the deformation mechanisms.

The observed trends revealed that influence of OWT weight on foundation settlement was primarily controlled by two controversial mechanisms. First, although heavier OWTs may intensify larger amount

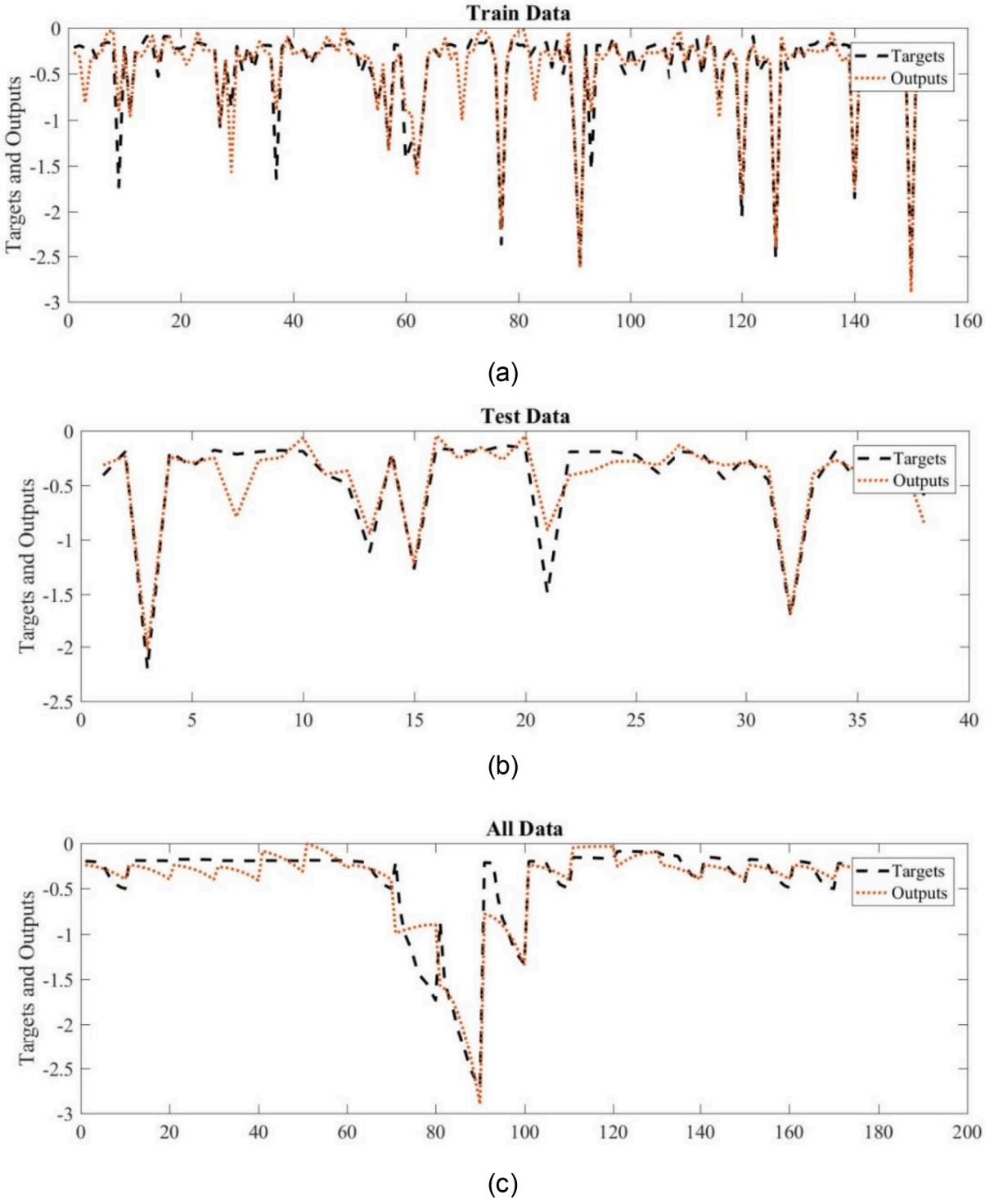

Fig. 27. Comparison between targets and outputs data a) Train Data b) Test Data c) All input D.

of EPWP generation and settlement mechanisms until a threshold limit (i.e. q >~ 100 kPa), a further increase in OWT weight adversely affected the foundation settlement. The higher values of EPWP may not be sufficiently high to compensate initial vertical effective stress.

Second, when skirt tip was situated in a thick liquefiable layer, foundation settlement was generally similar to pile settlement and as the OWT weight increased, the settlement increased.

Analyses on influence of skirt length and caisson diameter on foundation settlement confirmed that increasing skirt length effectively limits the settlement due to higher frictional resistance between skirt skin and surrounded soil. In contrast, the decreasing caisson diameter considerably increased the settlement due to the increase in contact pressure, if all else remains unchanged. It is worth mentioning that for all settlement analyses, higher specific densities resulted in smaller settlements.

Further, bearing capacity analyses demonstrated that occurrence of wave-induced liquefaction led to bearing capacity degradation. Skirted foundations are more resistant to loss of bearing capacity after the liquefaction due to the considerable inner frictional resistance of skirts, therefore caissons with longer skirts experienced smaller settlements.

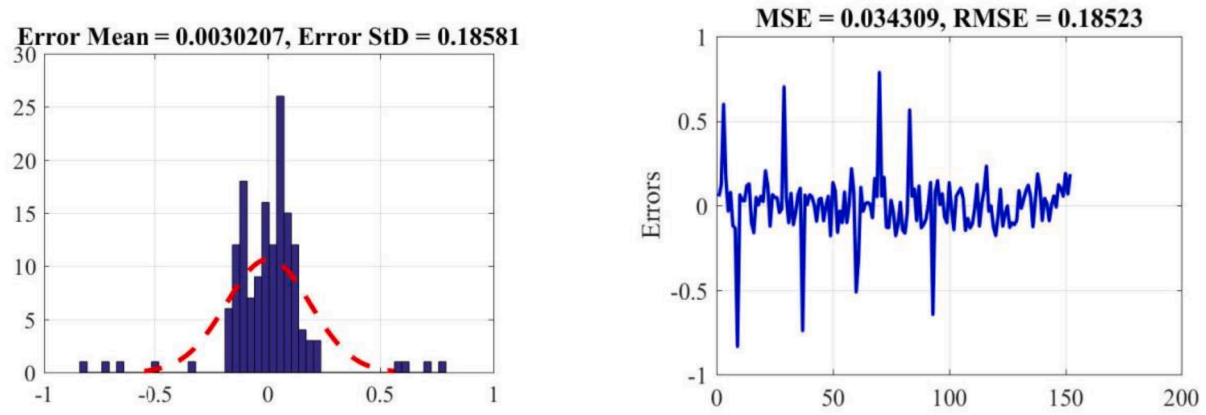

a) Train Data

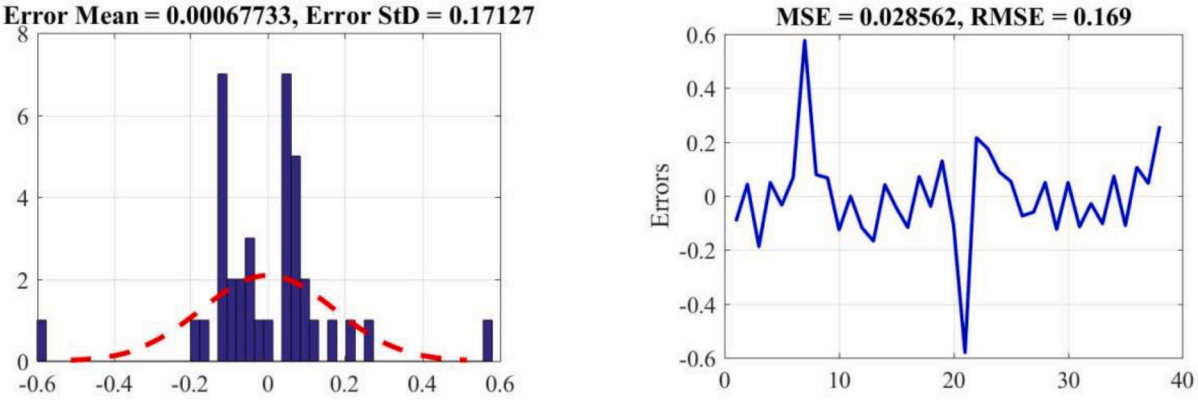

b) Test Data

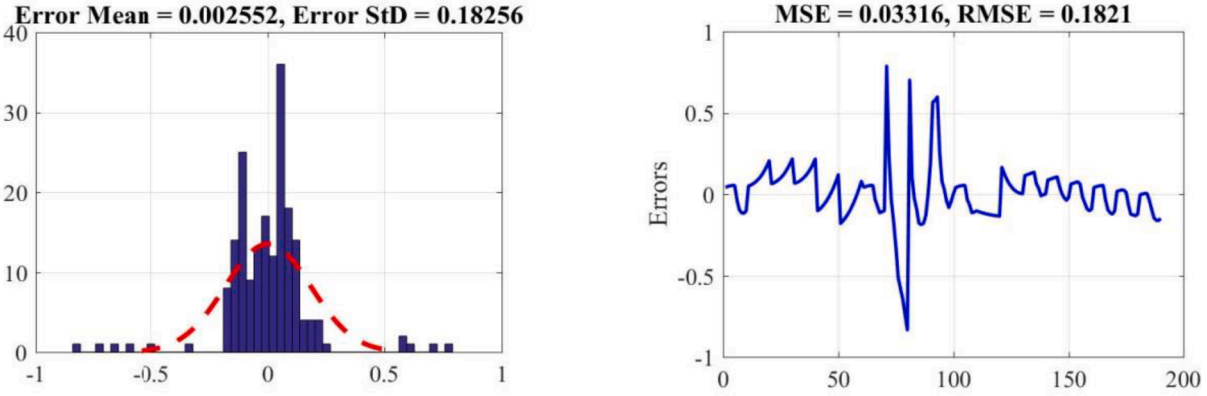

c) All input Data

Fig. 28. Histogram of standard deviation error and Histogram error for GMDH output.

Moreover, results showed that for denser sands, bearing capacity ratio of foundations were less sensitive to embedment ratio variation.

The presence of non-liquefiable layer at the bottom of seabed in relation to the fully- liquefiable deposit, was demonstrated to increase both the bearing capacity and degraded bearing capacity, thereby increasing the *BCR*.

A simplified procedure, based on the r_u generated by different wave characteristics, was developed to predict the *BCR* of offshore foundation under the action of waves. It is revealed that in spite of the high scatteredness of data for higher values of EPWPR, a quadratic function can reasonably predict the normalised degraded bearing capacity variation with development of EPWPR.

Finally, with the aid of artificial neural network approaches, an analytical framework is proposed for prediction of wave-induced caisson settlement using a dataset captured from the analysis of key model parameters affecting the foundation settlement with MSE and RMSE parameters as 0.034309 and 0.18523, respectively.

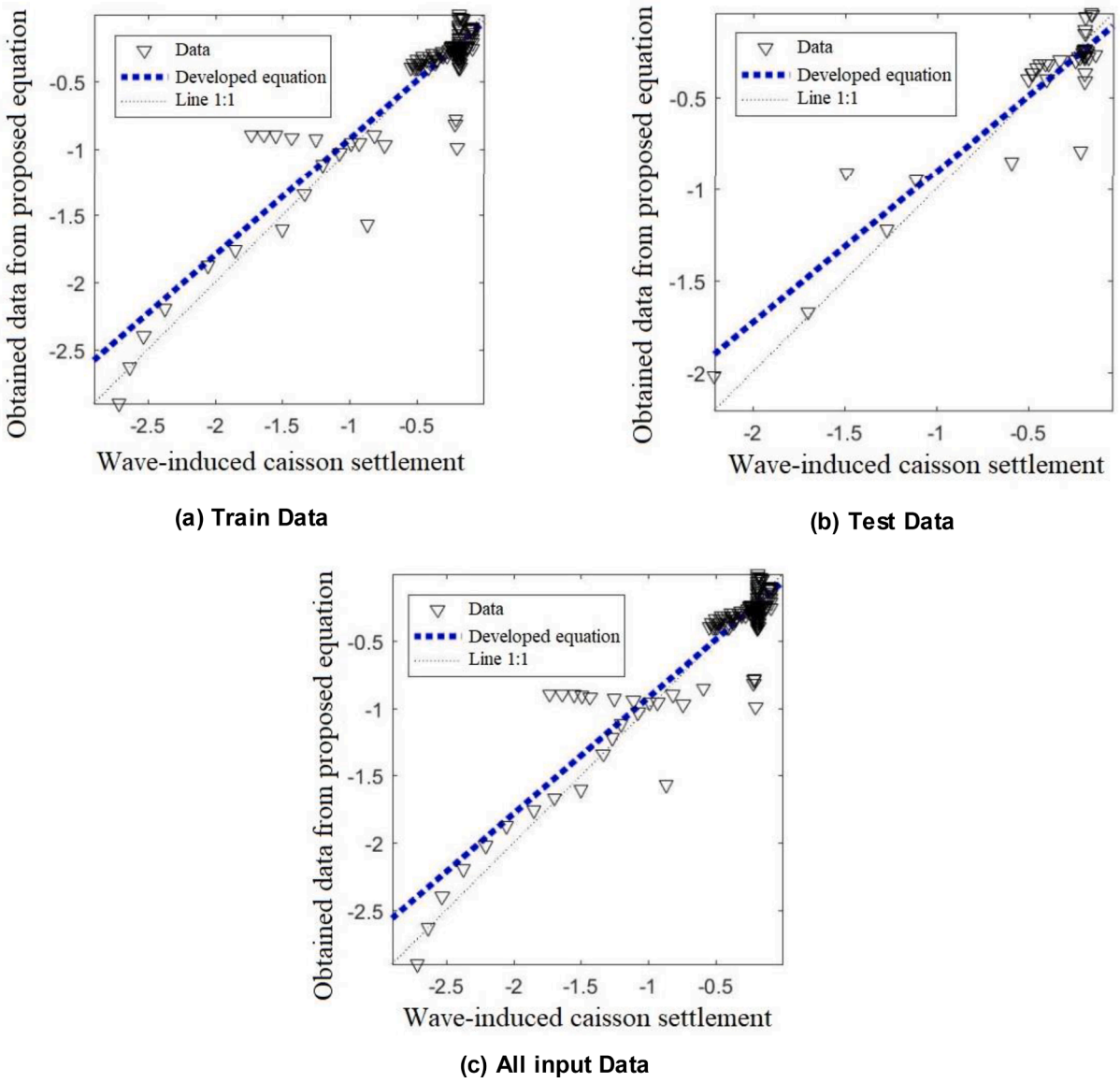

Fig. 29. Comparison of observed settlement from FE analysis results with those estimated from proposed Eq. (37).

CRediT authorship contribution statement

Amir Moghaddam: Conceptualization, Software, Investigation, Validation, Formal analysis, Investigation, Data curation, Writing – original draft, Visualization. **Amin Barari:** Conceptualization, Methodology, Writing – review & editing, Supervision, Project administration, Funding acquisition. **Sina Farahani:** Software, Formal analysis, Writing – review & editing, Visualization. **Alireza Tabarsa:** Resources, Writing – review & editing, Supervision. **Dong-Sheng Jeng:** Methodology, Writing – review & editing.

Declaration of Competing Interest

The authors declare that they have no known competing financial interests or personal relationships that could have appeared to influence the work reported in this paper.

Data availability

Data will be made available on request.

Acknowledgments

The authors gratefully acknowledge the financial support received from the European Union's Horizon 2020 research and innovation programme under grant agreement No 818153. This study is funded as part of i4Offshore project (Integrated Implementation of Industrial Innovations for Offshore Wind Cost Reduction).

Data availability

Some or all data, models, or code generated or used during the study are available from the corresponding author by request.

Appendix 1

Table A1 The inputs data for the training ANN network of wave-induced caisson settlement.

References

Achmus, M., Akdag, C.T., Thieken, K., 2013. Load-bearing behavior of suction bucket foundations in sand. Appl. Ocean Res. 43, 157–165.

Achmus, M., Kuo, Y.-S., Abdel-Rahman, K., Tseng, Y.H., Pang, I., 2020. Capacity degradation method for piles under cyclic axial loads. Comput. Geotech. 128, 103838.
Adalier, K., Elgamal, A.-W., Martin, G.R., 1998. Foundation Liquefaction Countermeasures for Earth Embankments. J. Geotech. Geoenviron. Eng. 124 (6), 500–517.
Ahidashti, R.A., Barari, A., Haddad, A., 2019. Insight into the post-liquefaction behaviour of skirted foundations, Earthquake Geotechnical Engineering for Protection and Development of Environment and Constructions, CRC Press, pp. 1106-1113.
Arulmoli, K., Muraleetharan, K.K., Hossain, M.M., Fruth, L.S., 1992. VELCAS verification of liquefaction analysesby centrifuge studies labratory testing program soil data report. National science foundation, Washington, D.C.
Bandara, S., Ferrari, A., Laloui, L., 2016. Modelling landslides in unsaturated slopes subjected to rainfall infiltration using material point method. Int. J. Numer. Anal. Meth. Geomech. 40 (9), 1358–1380.
Barari, A., Ibsen, L.B., Taghavi Ghalesari, A., Larsen, K.A., 2017b. Embedment Effects on Vertical Bearing Capacity of Offshore Bucket Foundations on Cohesionless Soil. Int. J. Geomech. 17 (4).
Barari, A., Ibsen, L.B., 2017. Insight into the lateral response of offshore shallow foundations. Ocean Eng. 144, 203–210.
Barari, A., Bagheri, M., Rouainia, M., Ibsen, L.B., 2017a. Deformation Mechanisms of Offshore Monopile Foundations Accounting for Cyclic Mobility Effects. Soil Dyn. Earthq. Eng. 97, 439–453. https://doi.org/10.1016/j.soildyn.2017.03.008.
Barari, A., Zeng, X., Rezania, M., Ibsen, L.B., 2021. Three-dimensional modeling of monopiles in sand subjected to lateral loading under static and cyclic conditions. Geomechanics and Engineering 26 (2), 175–190.
Barari, A., Glitrup, K., Christiansen, L.R., Ibsen, L.B., Choo, Y.W., 2021. Tripod suction caisson foundations for offshore wind energy and their monotonic and cyclic responses in silty sand: Numerical predictions for centrifuge model tests. Soil Dyn. Earthq. Eng. 149, 106813.
Bastidas, A., 2016. Ottawa F-65 Sand Characterization. University of California Davis, California.
Been, K., Jefferies, M.G., 1985. A state parameter for sands. A state parameter for sands. *Géotechnique* 35 (2), 99–112.
Bhattacharya, S., 2003. Pile instability during earthquake liquefaction. Thesis (Ph.D.), Geotechnical Engineering Group. Thesis (Ph.D.), University of Cambridge, UK.
Bienen, B., Gaudin, C.H., Cassidy, M., Rausch, L., Purwana, O.A., 2012. Numerical modeling of undrained capacity of hybrid skirted foundation under combined loading. Int. J. Offshore Polar Eng. 22 (4), 323–329.
Biot, M.A., 1941. General Theory of Three-Dimensional Consolidation. J. Appl. Phys. 12 (2), 155–164.
Boulanger, R.W., Seed, R.B., 1995. Liquefaction of Sand Under Bidirectional Monotonic and Cyclic Loading. J. Geotech. Eng. 121 (12), 870–878.
Castro, G., Poulos, S.J., 1977. Factors affecting liquefaction and cyclic mobility. Journal of Geotechnical Engineering Division, ASCE 103 (GT6), 501–516.
Cerato, B.A., 2005. Scale effects of shallow foundation bearing capacity on granular material. University of Massachusetts, Amherst, Mass, USA. Ph.D. thesis,.
Dafalias, Y.F., 1986. Bounding Surface Plasticity; Mathematical Foundation and Hypoplasticity. J. Eng. Mech. 112 (9), 966–987.
Davisson, M.T., Robinson, K.E., 1965. Bending and Buckling of Partially Embedded Piles. Soil Mech & Fdn Eng Conf Proc. 2, Canada: Proceedings of 6th ICSMFE, pp. 243-246.
De Alba, P.A., Chan, C.K., Seed, H.B., 1976. Sand Liquefaction in Large-Scale Simple Shear Tests. J. Geotech. Eng. Div. 102 (9).
Esfeh, P.K., Kaynia, A.M., 2020. Earthquake response of monopiles and caissons for Offshore Wind Turbines founded in liquefiable soil. Soil Dyn. Earthq. Eng. 136, 106213.
Farahani, S., Akhaveissy, A.H., 2022. Direct displacement-based seismic design of buckling-restrained braced RC frames. Bull. Earthq. Eng. 20 (3), 1767–1839.
Farlow, S.J., 2020. Self-organizing methods in modeling: GMDH type algorithms. CRC Press.
Gelagoti, F., Kourkoulis, R., Lekkakis, P.C., Kaynia, A., 2014. Suction caisson foundations for offshore wind turbines subjected to wave and earthquake loading: effect of soil-foundation interface. Géotechnique 64, 171–185.
Green, R.A., Wotherspoon, L., Cubrinovski, M., Bradshaw, A.S., 2011. Performance of Levees (Stopbanks) During the 4 September 2010, Mw7.1 Darfield and 22 February 2011, Mw6.2 Christchurch New Zealand Earthquakes. Seismological Research Letters, 82 (6), pp. 939-949.
Haddad, A., Barari, A., Amini, R., 2022. The remedial performance of suction caisson foundations for offshore wind turbines under seismically induced liquefaction in the seabed: shake table testing. Mar. Struct. 83, 103171.
Harder, L.F., Boulanger, R., 1997. Application of Kσ and Kα correction factors. Proceedings of the NCEER workshop on evaluation of liquefaction resistance of soils, report NCEER-97-0022. Buffalo, NY, USA: National Center for Earthquake Engineering Research, State University of New York, pp. 167-190.
Hausler, E., 2002. Influence of ground improvement on settlement and liquefaction: a study based on field case history evidence and dynamic geotechnical centrifuge tests. Univ. of Calif., Berkeley: Ph.D. Dissertation, Ch. 5, pp. 85-271.
Ibsen, L.B., Barari, A., Larsen, K.A., 2014. Adaptive plasticity model for bucket foundations. J. Eng. Mech. 140 (2), 361–373.
Ibsen, L.B., Larsen, K.A., Barari, A., 2014. Calibration of failure criteria for bucket foundations on drained sand under general loading. J. Geotech. Geoenviron. Eng. 140 (7), 04014033.
Ibsen, L.B., Barari, A., Larsen, K.A., 2015. Effect of embedment on the plastic behavior of bucket foundations. J. Waterw. Port Coast. Ocean Eng. 141 (6), 06015005.
Ishihara, K., Yamakazi, F., 1980. Cyclic Simple Shear Tests on Saturated Sand in Multi-Directional Loading. Soils Found. 20 (1), 45–59.
Ivakhnenko, A.G., 1971. Polynomial theory of complex systems. IEEE Trans. Syst. Man Cybern. SMC-1 (4), 364–378.
Jeng, D.S., Zhao, H.Y., 2014. Two-dimensional model for accumulation of pore pressure in marine sediments. J. Waterw. Port. Coast. Ocean. Eng. 141 (3), 04014042.
Jonkman, J., Butterfield, S., Musial, W., Scott, G., 2009. Definition of a 5-mw reference wind turbine for offshore system development. National Renewable Energy Laboratory.
Kammerer, A., Wu, J., Riemer, M., Pestana, J., Seed, R., 2004. A New Multi-directional Direct Simple Shear Testing Database. 13th World Conference on Earthquake Engineering. WCEE, Vancouver, B.C., Canada.
Karamitros, D.K., Bouckovalas, G.D., Chaloulos, Y.K., Andrianopoulos, K.I., 2013. Numerical analysis of liquefaction-induced bearing capacity degradation of shallow foundations on a two-layered soil profile. Soil Dyn. Earthq. Eng. 44, 90–101.
Karimi, Z., Dashti, S., Bullock, Z., Porter, K., Liel, A., 2018. Key predictors of structure settlement on liquefiable ground: a numerical parametric study. Soil Dyn. Earthq. Eng. 113, 286–308.
Kolay, P.K., Kumar, S., Tiwari, D., 2013. Improvement of bearing capacity of shallow foundation on Geogrid reinforced silty clay and sand. J. Constr. Eng. 2013, 1–10.
Kourkoulis, R., Georgiou, I., 2015. Seismic response of suction caissons: effect of two-directional loading. 6th International Conference on Earthquake Geotechnical Engineering. WCEE, Christchurch, New Zealand.
Li, X.S., Dafalias, Y.F., 2000. Dilatancy for cohesionless soils. Dilatancy for cohesionless soils. *Géotechnique* 50 (4), 449–460.
Li, Y., Ong, M.C., Tang, T., 2018. Numerical analysis of wave-induced poro-elastic seabed response around a hexagonal gravity-based offshore foundation. Coast. Eng. 136, 81–95.
Liu, L., Dobry, R., 1997. Seismic response of shallow foundation on liquefiable sand. J. Geotech. Geoenviron. Eng., ASCE 123 (6), 557–567.
Liu, H., Kemetzetzidis, E., Abell, J.A., Pisano, F., 2021. From cyclic sand ratcheting to tilt accumulation of offshore monopiles: 3D FE modelling using SANISAND-MS. Géotechnique.
McKenna, F., Fenves, G.L., Scott, M.H., Jeremic, B., 2000. Open system for earthquake engineering simulation (OpenSees). PEER Center: Univ. of California, Berkeley, CA, United States, http://opensees.berkeley.edu.
Miyamoto, J., Shinji, S., Tsurugasaki, K., Sumida, H., 2020. Wave-induced liquefaction and instability of offshore monopile in a drum centrifuge. Soils Found.
Moghaddam, A., Barari, A., Tabarsa, A., 2020. Mechanism of wave-induced liquefaction around suction caissons. 73rd Canadian Geotechnical Conference. CGS, GeoVirtual2020.
Nariman-Zadeh, N., Darvizeh, A., Darvizeh, M., Gharababaei, H., 2002. Modelling of explosive cutting process of plates using GMDH-type neural network and singular value decomposition. J. Mater. Process. Technol. 128 (1–3), 80–87.
Nazarimofrad, E., Farahani, S., Zahrai, S.M., 2019. Multiobjective optimal placement of active tendons to control irregular multistory buildings with soil–structure interaction. Struct. Design Tall Spec. Build. 28 (4).
Palacios, A., Nguyen, D.M., Markovic, V., Farahani, S., Barari, A., Ibsen, L.B., 2022. Numerical simulation of caisson-supported offshore wind turbines involving uniform liquefiable sand layer. (pp. 4th International Conference on Performance-Based Design in Earthquake Geotechnical Engineering (PBD-IV)). Beijing, China.
Poulos, H.G., 1989. Cyclic axial loading analysis of piles in sand. ASCE J. Geotech. Eng. 115 (6), 836–852.
Sassa, S., Sekiguchi, H., 1999. Wave-induced liquefaction of beds of sand in a centrifuge. Géotechnique 49 (5), 621–638.
Seed, R.B., Harder, L.F., 1990. SPT-based analysis of cyclic pore pressure generation and undrained residual strength. In: Duncan, J.M. (ed.), Proceedings of the Seed memorial symposium, pp. 351-376.
Seed, H.B., Rahman, M.S., 1978. Wave-induced pore pressure in relation to ocean floor stability of cohesionless soils. Mar. Geotechnol. 3 (2), 123–150.
Skau, K.S., Chen, Y., Jostad, H.P., 2018. A numerical study of capacity and stiffness of circular skirted foundations in clay subjected to combined static and cyclic general loading. Géotechnique 68 (3), 205–220.
Stapelfeldt, M., Bienen, B., Grabe, J., 2020. The influence of the drainage regime on the installation and the response to vertical cyclic loading of suction caissons in dense sand. Ocean Eng. 215, 107105.
Stapelfeldt, M., Bienen, B., Grabe, J., 2021. Influence of Low-Permeability Layers on the Installation and the Response to Vertical Cyclic Loading of Suction Caissons. J. Geotech. Geoenviron. Eng. 147 (8).
Sui, T., Zhang, C., Jeng, D., Guo, Y., Zheng, J., Zhang, W., Shi, J., 2019. Wave-induced seabed residual response and liquefaction around a mono-pile foundation with various embedded depth. Ocean Eng. 173, 157–173.
Sumer, B.M., Fredsøe, J., 2002. The Mechanics of Scour in the Marine Environment (Vol. 17). World Scientific, Advanced Series on Ocean Engineering.
Sumer, B.M., 2014. Liquefaction around marine structures. Singapore: World Scientific, Advanced Series On Ocean Engineering.
Suryasentana, S.K., Burd, H.J., Byrne, B.W., Shonberg, A., 2020. A Winkler model for suction caisson foundations in homogeneous and non-homogeneous linear elastic soil. Géotechnique 1–17.
Tasiopoulou, P., Chaloulos, Y., Gerolymos, N., Giannakou, A., Chacko, J., 2021. Cyclic lateral response of OWT bucket foundations in sand: 3D coupled effective stress analysis with Ta-Ger model. Soils Found. 61 (2), 371–385.
Vaid, Y.P., Chern, J.C., 1983. Effect of static shear on resistance to liquefaction. Soils Found. 23 (1), 43–60.
Vaid, Y.P., Stedman, J.D., Sivathayalan, S., 2001. Confining stress and static shear stress effects in cyclic liquefaction. Can. Geotech. J. 38 (3), 580–591.
Vincent, S., Kim, S.R., Hung, L.C., 2020. Evaluation of horizontal and vertical bearing capacities of offshore bucket work platforms in sand. Appl. Ocean Res. 101, 102198.

Wang, X., Zhang, J., 2016. Dynamic behaviors of saturated seabed soils induced by different kinds of waves. *OCEANS-2016*, IEEE, Shanghai, China, pp. 1-6.
Wang, Z.L., Dafalias, Y.F., Shen, C.K., 1990. Bounding surface hypoplasticity model for sand. J. Eng. Mech. 116 (5), 983–1001.
Wang, R., Zhang, J.-M., Wang, G., 2014. A unified plasticity model for large post-liquefaction shear deformation of sand. Comput. Geotech. 59, 54–66.
Wang, R., Fu, P., Zhang, J.-M., 2016. Finite element model for piles in liquefiable ground. Comput. Geotech. 72, 1–14.
Wang, X., Zhang, J.-M., 2018. Interaction of Pipeline and Elasto-Plastic Sandy Seabed Under Dynamic Loadings. The 28th International Ocean and Polar Engineering Conference. International Society of Offshore and Polar Engineers, Sapporo, Japan.
Wang, X., Yang, X., Zeng, X., 2017. Seismic centrifuge modelling of suction bucket foundation for offshore wind turbine. Renew. Energy 114, 1013–1022.
Wei, H., Chen, J.-S., Beckwith, F., Baek, J., 2020. A naturally stabilized semi-lagrangian meshfree formulation for multiphase porous media with application to landslide modeling. J. Eng. Mech. 146 (4).
Yamamoto, T., Koning, H.L., Sellmeijer, H., Hijum, E.V., 1978. On the response of a poro-elastic bed to water waves. J. Fluid Mech. 87 (1), 193–206.
Yang, Z., Lu, J., Elgamal, A.-W., 2008. OpenSees Soil Models and Solid-Fluid Fully Coupled Elements. OpenSees User's Manual, UC San Diego.
Zen, K., Yamazaki, H., 1990. Mechanism of wave-induced liquefaction and densification in seabed. Soils Found. 30 (4), 90–104.
Zhang, J.-M., Wang, G., 2012. Large post-liquefaction deformation of sand, part I: physical mechanism, constitutive description and numerical algorithm. Acta Geotech. 7 (2), 69–113.
Zhang, C., Zhang, Q., Wu, Z., Zhang, J., Sui, T., Wen, Y., 2015. Numerical Study on Effects of the Embedded Monopile Foundation on Local Wave-Induced Porous Seabed Response. Math. Probl. Eng. 2015, 1–13.
Zhang, J.-F., Zhang, X.-N., Yu, C., 2016. Wave-induced seabed liquefaction around composite bucket foundations of offshore wind turbines during the sinking process. J. Renew. Sustainable Energy 8 (2).
Zhao, L., Bransby, M.F., Gaudin, C., Cassidy, M.J., 2020. Capacity of caissons in dense sand under combined loading. J. Geotech. Geoenviron. Eng. 146 (4).
Zhao, H.Y., Jeng, D.S., Liao, C.C., Zhu, J.F., 2017. Three-dimensional modeling of wave-induced residual seabed response around a mono-pile foundation. Coast. Eng. 128, 1–21.
Zhu, F.Y., Bienen, B., O'Loughlin, C., Cassidy, M.J., Morgan, M., 2019. Suction caisson foundations for offshore wind energy: cyclic response in sand and sand over clay. Géotechnique 69 (10), 924–931.
Zhu, B., Ren, J., Ye, G.-L., 2018. Wave-induced liquefaction of the seabed around a single pile considering pile–soil interaction. Mar. Georesour. Geotechnol. 36 (1), 150–162.
Zienkiewicz, O.C., Shiomi, T., 1984. Dynamic behaviour of saturated porous media; The generalized Biot formulation and its numerical solution. Int. J. Numer. Anal. Meth. Geomech. 8 (1), 71–96.
Zienkiewicz, O.C., Chang, C.T., Bettess, P., 1980. Drained, undrained, consolidating and dynamic behaviour assumptions in soils. Géotechnique 30 (4), 385–395.
Ziotopoulou, K., Montgomery, J., Bastidas, A., Morales, B., 2018. Cyclic Strength of Ottawa F-65 Sand: Laboratory Testing and Constitutive Model Calibration. Geotechnical Earthquake Engineering and Soil Dynamics Conference GEESD. Austin, TX.